



# Aerosol retrievals from different polarimeters during the ACEPOL campaign using a common retrieval algorithm

Guangliang Fu<sup>1</sup>, Otto Hasekamp<sup>1</sup>, Jeroen Rietjens<sup>1</sup>, Martijn Smit<sup>1</sup>, Antonio Di Noia<sup>2</sup>, Brian Cairns<sup>3</sup>, Andrzej Wasilewski<sup>4</sup>, David Diner<sup>5</sup>, Felix Seidel<sup>5</sup>, Feng Xu<sup>6</sup>, Kirk Knobelspiesse<sup>7</sup>, Meng Gao<sup>7</sup>, Arlindo da Silva<sup>7</sup>, Sharon Burton<sup>8</sup>, Chris Hostetler<sup>8</sup>, John Hair<sup>8</sup>, and Richard Ferrare<sup>8</sup>

<sup>1</sup>Netherlands Institute for Space Research (SRON, NWO-I), Utrecht, the Netherlands

<sup>2</sup>Department of Physics and Astronomy, University of Leicester, Leicester, LE1 7RH, UK

<sup>3</sup>NASA Goddard Institute for Space Studies (GISS), New York, USA

<sup>4</sup>Trinnovim LLC., New York, USA

<sup>5</sup>NASA Jet Propulsion Laboratory (JPL), California Institute of Technology, Pasadena, USA

<sup>6</sup>School of Meteorology, The University of Oklahoma National Weather Center, Norman, USA

<sup>7</sup>NASA Goddard Space Flight Center, Greenbelt, USA

<sup>8</sup>NASA Langley Research Center, Hampton, USA

**Correspondence:** Guangliang Fu (g.fu@sron.nl) and Otto Hasekamp (o.hasekamp@sron.nl)

Received: 23 July 2019 – Discussion started: 29 July 2019

Revised: 6 December 2019 – Accepted: 31 December 2019 – Published: 7 February 2020

**Abstract.** In this paper, we present aerosol retrieval results from the ACEPOL (Aerosol Characterization from Polarimeter and Lidar) campaign, which was a joint initiative between NASA and SRON – the Netherlands Institute for Space Research. The campaign took place in October–November 2017 over the western part of the United States. During ACEPOL six different instruments were deployed on the NASA ER-2 high-altitude aircraft, including four multi-angle polarimeters (MAPs): SPEX airborne, the Airborne Hyper Angular Rainbow Polarimeter (AirHARP), the Airborne Multi-angle SpectroPolarimetric Imager (AirMSPI), and the Research Scanning Polarimeter (RSP). Also, two lidars participated: the High Spectral Resolution Lidar-2 (HSRL-2) and the Cloud Physics Lidar (CPL). Flights were conducted mainly for scenes with low aerosol load over land, but some cases with higher AOD were also observed. We perform aerosol retrievals from SPEX airborne, RSP (410–865 nm range only), and AirMSPI using the SRON aerosol retrieval algorithm and compare the results against AERONET (Aerosol RObotic NETwork) and HSRL-2 measurements (for SPEX airborne and RSP). All three MAPs compare well against AERONET for the aerosol optical depth (AOD), with a mean absolute error (MAE) between 0.014 and 0.024 at 440 nm. For the fine-mode effective radius the MAE ranges between 0.021

and 0.028  $\mu\text{m}$ . For the comparison with HSRL-2 we focus on a day with low AOD (0.02–0.14 at 532 nm) over the California Central Valley, Arizona, and Nevada (26 October) as well as a flight with high AOD (including measurements with AOD > 1.0 at 532 nm) over a prescribed forest fire in Arizona (9 November). For the day with low AOD the MAEs in AOD (at 532 nm) with HSRL-2 are 0.014 and 0.022 for SPEX and RSP, respectively, showing the capability of MAPs to provide accurate AOD retrievals for the challenging case of low AOD over land. For the retrievals over the smoke plume a reasonable agreement in AOD between the MAPs and HSRL-2 was also found (MAE 0.088 and 0.079 for SPEX and RSP, respectively), despite the fact that the comparison is hampered by large spatial variability in AOD throughout the smoke plume. A good comparison is also found between the MAPs and HSRL-2 for the aerosol depolarization ratio (a measure of particle sphericity), with an MAE of 0.023 and 0.016 for SPEX and RSP, respectively. Finally, SPEX and RSP agree very well for the retrieved microphysical and optical properties of the smoke plume.

## 1 Introduction

Aerosols such as smoke, sulfate, dust, and volcanic ash particles affect the Earth climate directly by interaction with radiation and indirectly by modifying the cloud properties. In contrast to the warming effect of greenhouse gases, which is understood quite well, the quantification of aerosol cooling contains a large uncertainty, as reported in the latest (5th) assessment report of the Intergovernmental Panel on Climate Change (IPCC, 2014). This large uncertainty adds substantial difficulties in the prediction of the Earth's climate change in the future. Aerosols also have a big influence on air quality. Air pollution from aerosols may result in severe adverse problems to human health (Wyzga and Rohr, 2015). To improve our understanding of the aerosol effect on climate and air quality, accurate global measurements of aerosol optical properties (e.g., aerosol optical depth – AOD; single-scattering albedo – SSA), microphysical properties (size distribution, refractive index, particle shape), and their vertical distribution are of crucial importance. Satellite instruments are needed to obtain such measurements at a global scale.

Lidar measurements are needed to obtain vertical profile information about aerosols. The Cloud–Aerosol Lidar with Orthogonal Polarization (CALIOP) elastic backscatter lidar (Winker et al., 2010) has been providing aerosol lidar measurements since 2006. High-spectral-resolution lidar (HSRL) techniques (Hair et al., 2008) are being used for the new generation of lidar instrumentation such as the Cloud–Aerosol Transport System (CATS) instrument (Yorks et al., 2014), which was operational on the International Space Station (ISS) in the period 2015–2017, and for the European Space Agency (ESA) Earthcare mission (Illingworth et al., 2014), expected for launch in 2021. In comparison to elastic backscatter lidars, the HSRL technique has an additional filtered channel that provides an assessment of aerosol extinction. It also improves the accuracy of the aerosol backscatter profile, especially at altitudes far from the instrument, since it is calculated as a direct ratio of two channels instead of being retrieved with assumptions that result in accumulating errors. The HSRL methodology also improves aerosol depolarization through improved backscatter and provides the aerosol lidar ratio using the extinction (Burton et al., 2012).

From a passive remote sensing point of view, instruments that measure both intensity and polarization and observe a ground pixel under multiple viewing angles contain the richest set of information about aerosols in our atmosphere (Dubovik et al., 2019). The reason is that the angular dependence of the scattering matrix elements related to linear polarization depend strongly on the microphysical aerosol properties, like refractive index and particle size (Hansen and Travis, 1974; Mishchenko and Travis, 1997). Furthermore, the polarization signal is mostly dominated by light that has been scattered only once, which means that the characteristics of the scattering matrix remain largely preserved in a top-of-atmosphere polarization measurement. The added value

of polarization has been demonstrated by a number of studies on synthetic measurements (Mishchenko and Travis, 1997; Hasekamp and Landgraf, 2007; Hasekamp, 2010; Knobelspiesse et al., 2012), airborne measurements (Chowdhary et al., 2005; Waquet et al., 2009; Xu et al., 2017; Wu et al., 2015, 2016; Fan et al., 2019), and spaceborne measurements (Hasekamp et al., 2011; Dubovik et al., 2011; Fu and Hasekamp, 2018). These algorithms can be divided into two main groups: approaches based on a lookup table (LUT) (Deuzé et al., 2000; Deuzé et al., 2001; Herman et al., 1997; Waquet et al., 2016) and full inversion approaches (Dubovik et al., 2011; Hasekamp and Landgraf, 2007; Hasekamp et al., 2011; Stap et al., 2015; Wu et al., 2015, 2016; Di Noia et al., 2017; Fu and Hasekamp, 2018; Xu et al., 2017; Waquet et al., 2009; Stamnes et al., 2018). Generally speaking, LUT approaches are faster but less accurate than full inversion approaches because LUT approaches choose the best-fitting aerosol model from a discrete lookup table. Full inversion approaches are more accurate but slower because they require radiative transfer calculations as part of the retrieval procedure. It should be noted that of the full inversion approaches only the SRON-Aerosol algorithm and the GRASP algorithm have been applied at a global scale.

The best known satellite instruments that performed multi-angle photopolarimetric measurements of the Earth atmosphere were the POLDER (Polarization and Directionality of the Earth's Reflectances) instruments (Deschamps et al., 1994), of which the recently decommissioned POLDER-3 onboard the PARASOL micro-satellite provided data from 2005 to 2013. Although the original algorithms for aerosol retrieval from POLDER-3 do not make full use of the information contained in the MAP measurements (Deuzé et al., 2000, 2001), algorithms developed more recently (Dubovik et al., 2011; Hasekamp et al., 2011; Fu and Hasekamp, 2018) do fully exploit the available information and provide insight into the capabilities and limitations of the POLDER-3 instrument. The advanced data products of these algorithms have been applied at a global (Lacagnina et al., 2015, 2017; Hasekamp et al., 2019b) and regional (Chen et al., 2018) scale. The main limitation of the POLDER instruments is the limited accuracy with which the degree of linear polarization (DoLP) can be measured. The DoLP accuracy is intrinsically limited by the filter wheel technology, which relies on sequential measurements of different polarization directions, in combination with a spatial under-sampling. On the other hand, the advantage of this technology is that it allows for a large swath with (almost) global coverage in a day. The POLDER design also forms the blueprint for the 3MI instruments (Fougnie et al., 2018), to be flown on METOP-SG in the time frame  $\sim 2020$  to 2035.

Focus for the development of new polarimetric instrumentation has been on improved polarimetric accuracy, more viewing angles, more wavelengths, an extended spectral range, or a combination of these aspects. For a number of these instrument concepts airborne demonstrators for possi-

ble future satellite missions have been built: (1) the Research Scanning Polarimeter (RSP) (Cairns et al., 2004), which is an airborne version of the Aerosol Polarimetry Sensor (APS) (Mishchenko et al., 2007) that was lost in a failed launch in 2011. RSP measures at many viewing angles ( $\sim 150$ ) and nine wavelength bands between 410 and 2250 nm. It has a demonstrated DoLP accuracy of better than 0.002 (Knobelspiesse et al., 2019). (2) The Airborne Multi-angle SpectroPolarimetric Imager (AirMSPI) (Diner et al., 2013) is an eight-band (355, 380, 445, 470, 555, 660, 865, 935 nm) push-broom camera measuring polarization in the 470, 660, and 865 nm bands mounted on a gimbal to acquire multi-angular observations over a  $\pm 67^\circ$  along-track range. The AirMSPI concept will be implemented in a satellite mission as the Multi-Angle Imager for Aerosols (MAIA) to be launched in  $\sim 2021$  (Diner et al., 2018). (3) The Airborne Hyper-Angular Rainbow Polarimeter (AirHARP) (Martins et al., 2018) is a wide field-of-view imager that measures in the spectral bands at 440, 550, 670, and 865 nm; 670 nm is measured under 60 and the other bands under 20 viewing geometries. This concept will be implemented in a satellite instrument for a CubeSat mission to be launched in 2019 and for the Phytoplankton Aerosol Cloud and ocean Ecosystems (PACE) mission to be launched in 2022 (Werdell et al., 2019). (4) The Spectropolarimeter for Planetary Exploration (SPEX airborne) instrument (Smit et al., 2019) employs the spectral modulation technique (Snik et al., 2009) to accurately measure the DoLP with a spectral resolution of 10–20 nm. The intensity is being measured at a higher spectral resolution of 2–3 nm. SPEX airborne performs multi-angle measurements at nine viewing angles ranging  $\pm 56^\circ$  in a spectral range between 400 and 800 nm. The SPEX concept will be implemented in the satellite instrument SPEXone (Hasekamp et al., 2019a) for the NASA PACE mission (Werdell et al., 2019).

All four airborne MAPs listed above were mounted on the NASA Earth Resources-2 (ER-2) high-altitude ( $\sim 20$  km) aircraft (Navarro, 2007) during the Aerosol Characterization from Polarimeter and Lidar (ACEPOL) campaign, which was performed from October to November 2017, starting from the NASA Armstrong air base in Palmdale, California. During ACEPOL, two lidars were also deployed on the ER-2: the High Spectral Resolution Lidar-2 (HSRL-2) (Hair et al., 2008), providing vertically resolved measurements of backscatter coefficients (at 355, 532, and 1064 nm), extinction coefficients (at 355 and 532 nm), and the depolarization ratio (at 355, 532, and 1064 nm), and the Cloud Physics Lidar (CPL) (McGill et al., 2002), providing vertically resolved measurements of backscatter coefficients at 355, 532, and 1064 nm and the depolarization ratio at 1064 nm.

The goals of the ACEPOL campaign include the following: (i) comparison of level 1 (radiance and DoLP) performance between the different MAPs, (ii) comparison of aerosol retrievals from the different MAPs, (iii) comparing MAP retrievals to lidar retrievals, and (iv) performing combined retrievals using both MAP and lidar measure-

ments. The focus of this paper is on aspects (ii) and (iii): we will perform aerosol retrievals from RSP, SPEX airborne, and AirMSPI measurements during ACEPOL and evaluate the retrievals against AERONET (Aerosol RObotic NETWORK) and against HSRL-2. Note that aerosol retrievals from AirHARP measurements are not included in this paper because the data were not available when performing the analysis presented here.

In this study, we evaluate the performance of the different MAPs for retrieving aerosol optical and microphysical properties and also their capabilities to provide lidar-related aerosol properties. The retrieved aerosol properties are validated and compared with the data from AERONET and HSRL-2. The paper is organized as follows. Section 2 introduces the methodologies of the SRON algorithm for polarimetric aerosol retrievals, Sect. 3 describes the data sets from the ACEPOL campaign, which are used in this study, and the retrievals of different MAPs from ACEPOL are performed and compared with AERONET and HSRL-2 in Sect. 4. Finally, the last section summarizes and concludes this study.

## 2 Methodology

### 2.1 SRON multimode retrieval algorithm

In this paper, we employ the SRON aerosol retrieval algorithm in a multimode setup (Fu and Hasekamp, 2018). In principle, the idea of the multimode approach is that instead of fitting the size distribution parameters (the effective radius  $r_{\text{eff}}$  and the effective variance  $v_{\text{eff}}$ ) of two modes, one aims to fit the size distribution with a larger number of modes for which  $r_{\text{eff}}$  and  $v_{\text{eff}}$  are fixed. The advantage of this approach is that it makes the inversion problem more linear since  $r_{\text{eff}}$  and  $v_{\text{eff}}$  tend to make the inversion highly nonlinear. Another advantage is that the multimode approach has more freedom in fitting different shapes of the size distribution if the number of chosen modes is sufficiently large. In this paper, multimode retrievals based on five modes are used, and the aerosol size distribution is described in Table 1 (Fu and Hasekamp, 2018). We consider modes 1–3 together as the fine mode and modes 4 and 5 together as the coarse mode. To account for spectral dependence, we describe the refractive index  $m$  for the fine and coarse mode as  $m(\lambda) = \sum_{k=1}^n \alpha_k m^k(\lambda)$ , where  $m^k(\lambda)$  represents prescribed refractive indices as a function of wavelength and  $\alpha_k$  represents coefficients to be determined in the retrieval (see below). Both the real part and imaginary part of refractive indices are represented in this way. Here, we base the spectral dependence of the refractive index on the standard types of D'Almeida et al. (1991) (inorganic–sulfate, black carbon, and dust). The coefficients  $\alpha_k$  are the real numbers between 0 and 1 and are defined as weighting factors to combine the refractive index spectra for different aerosol components, e.g., DUST, water (H<sub>2</sub>O), black carbon (BC), and inorganic mat-

**Table 1.** Definition of the effective radius ( $r_{\text{eff}}$ ) and the effective variance ( $v_{\text{eff}}$ ) in the SRON five-mode retrieval.

	Mode 1	Mode 2	Mode 3	Mode 4	Mode 5
$r_{\text{eff}}$ ( $\mu\text{m}$ )	0.094	0.163	0.282	0.882	1.759
$v_{\text{eff}}$	0.130	0.130	0.130	0.284	1.718

ter (INORG). In this study, we set  $n_\alpha = 2$  and assume that the spectral dependence of the fine-mode and the coarse-mode refractive indices can be respectively described by IN-ORG+BC and DUST+INORG. Note that this assumption is flexible and can be updated according to the information content of the measurement. Spectra based on principal component analysis (PCA) can also be used as in Wu et al. (2015). The standard refractive index spectra are only used to describe the spectral dependence as the MAP measurements do not contain sufficient information to retrieve the refractive index for each wavelength separately. Nonspherical aerosols are described as a size–shape mixture of randomly oriented spheroids (Hill et al., 1984; Mishchenko et al., 1997). We use the Mie- and T-matrix-improved geometrical optics database by Dubovik et al. (2006) along with their proposed spheroid aspect ratio distribution for computing optical properties for a mixture of spheroids and spheres. The aerosol parameters included in the retrieval state vector  $\mathbf{x}$  are the aerosol column numbers for the five modes (Table 1), two coefficients (inorganic, black carbon) for the fine-mode refractive index, two coefficients (inorganic, dust) for the coarse-mode refractive index, the fraction of spherical particles (assumed the same for all modes), and the central height of a Gaussian aerosol height distribution (assumed the same for all modes).

For the surface reflection matrix we use (Rahman et al., 1993; Litvinov et al., 2011; Xu et al., 2017)

$$\mathbf{R}_s(\lambda, \mu_{\text{in}}, \mu_{\text{out}}, \phi_v - \phi_0) = A(\lambda) \left( \frac{(\mu_{\text{in}}\mu_{\text{out}})^{k-1}}{(\mu_{\text{in}} + \mu_{\text{out}})^{1-k}} F(g, \Theta) [1 + R(G)] \right) \mathbf{D} + \mathbf{R}_{\text{pol}}, \quad (1)$$

$$\mathbf{R}_{\text{pol}}(\mu_{\text{in}}, \mu_{\text{out}}, \phi_v - \phi_0) = B \left( \frac{\exp(-\tan(\frac{\pi-\Theta}{2})) \exp(-\nu) F_p(m, \Theta)}{4(\mu_{\text{in}} + \mu_{\text{out}})} \right), \quad (2)$$

where  $k$  is a parameter that varies between 0 and 1. This parameter controls the slope of the reflectance with respect to the illumination and view angles (Rahman et al., 1993).  $\mathbf{D}$  is the null matrix except  $\mathbf{D}_{11} = 1$ . The first part in Eq. (1) accounts for the bidirectional reflectance distribution function (BRDF) parameterized by the Rahman–Pinty–Verstraete (RPV) model (Rahman et al., 1993). The pairs  $(\theta_0, \phi_0)$  and  $(\theta_v, \phi_v)$  respectively denote the solar and viewing zenith and azimuth angles.  $\mu_{\text{in}}$  and  $\mu_{\text{out}}$  are respectively the cosines of incoming and outgoing angles.  $g$  is the asymmetry parameter of the Henyey–Greenstein phase function  $F(g, \Theta)$ .  $\Theta$  is the scattering angle.  $1 + R(G)$  is an ap-

proximation of the hot spot effect (Rahman et al., 1993), where  $G = \sqrt{\tan^2 \theta_0 + \tan^2 \theta_v - 2 \tan \theta_0 \tan |\theta_v| \cos(\phi_v - \phi_0)}$  and  $R(G) = \frac{1-A(\lambda)}{1+G}$ . The second part in Eq. (1) accounts for the surface polarized reflectance, for which we use the model proposed by Maignan et al. (2009).  $\mathbf{R}_{\text{pol}}$  is expressed by Eq. (2) (as stated by Eq. 31 in Litvinov et al., 2011). Here,  $B$  is a scaling parameter (band independent).  $F_p(m, \Theta)$  is the element  $F_{21}$  of the Fresnel scattering matrix with refractive index  $m$ . Parameter  $\nu$  is taken based on the atmospherically resistant vegetation index (ARVI) (Kaufman and Tanre, 1992). Here we use  $\nu = 0.6$ . Based on Eqs. (1) and (2), we include  $A(\lambda)$  at each measured wavelength and  $k$ ,  $g$ , and  $B$  as fit parameters in the state vector. In this paper, we perform aerosol retrievals from SPEX airborne, RSP, and AirMSPI, and the state vectors corresponding to these three polarimeters are listed in Table 2.

The measurement vector  $\mathbf{y}$  contains the measured radiances (sun normalized) and degree of linear polarization (DoLP) values at the different wavelengths and viewing angles. To retrieve the state vector from the measurements, a damped Gauss–Newton iteration method with Phillips–Tikhonov regularization is employed (Hasekamp et al., 2011; Fu and Hasekamp, 2018). The inversion algorithm finds the solution  $\hat{\mathbf{x}}$ , which solves the minimization-optimization problem,

$$\hat{\mathbf{x}} = \min_{\mathbf{x}} \left( \|\mathbf{S}_y^{-\frac{1}{2}} (\mathbf{F}(\mathbf{x}) - \mathbf{y})\|^2 + \gamma^2 \|\mathbf{W}^{-\frac{1}{2}} (\mathbf{x} - \mathbf{x}_a)\|^2 \right). \quad (3)$$

Here,  $\mathbf{F}$  is the forward model that simulates the measurement for a given state vector  $\mathbf{x}$ .  $\mathbf{F}$  consists of a radiative transfer model, for which we use the SRON radiative transfer model LINTRAN (Landgraf et al., 2001; Hasekamp and Landgraf, 2002, 2005; Schepers et al., 2014). All the radiative transfer calculations are performed for a model atmosphere that includes Rayleigh scattering, scattering and absorption by aerosols, and gas absorption. Rayleigh scattering cross sections are used from Bucholtz (1995). The forward model simulates Stokes parameters  $I$ ,  $Q$ , and  $U$  at the height of the observation (e.g.,  $\sim 20$  km for NASA ER-2 in this paper) for given optical properties (scattering and absorption optical thickness and scattering phase matrix for each vertical layer of the model atmosphere; 15 layers of the atmosphere are assumed). The other part of the forward model computes the optical properties from the aerosol microphysical properties using the tabulated kernels of Dubovik et al. (2006) for a mixture of spheroids and spheres.

Since the forward model is nonlinear the inversion problem has to be solved iteratively by replacing the forward model in each iteration step by its linear approximation,

$$\mathbf{F}(\mathbf{x}) \approx \mathbf{F}(\mathbf{x}_n) + \mathbf{K}(\mathbf{x} - \mathbf{x}_n). \quad (4)$$

Here,  $\mathbf{K}$  is the Jacobian matrix (with  $K_{ij} = \frac{\partial F_i}{\partial x_j}(\mathbf{x}_n)$ ), which contains the derivatives of the forward model with respect to

**Table 2.** Viewing angles and wavelengths used in retrievals among SPEX airborne, RSP, and AirMSPI, as well as the retrieved parameters from them. Prior values and weighting factors for the state vector are also listed in the table. In this paper, five-mode retrieval is used, and thus  $n_{\text{mode}} = 5$ . The arrows  $\rightarrow$ ,  $\leftarrow$ , or  $\uparrow$  indicate the same value with the arrow direction. The prior value and weighting factor of aerosol loading for each mode are calculated based on Mie theory using the prior information of AOD from the table (listed in the row of aerosol loading).

Polarimeters	SPEX airborne	RSP	AirMSPI		
Viewing angles	$\pm 56^\circ, \pm 42^\circ, \pm 28^\circ, \pm 14^\circ$ , and $0^\circ$ ( $n_{\text{vza}}^{\text{spex}} = 9$ )	Averaged based on $\sim 150$ angles ( $n_{\text{vza}}^{\text{rsp}} = 10$ )	$\pm 66^\circ, \pm 59^\circ, \pm 48^\circ, \pm 29^\circ$ , and $0^\circ$ ( $n_{\text{vza}}^{\text{airmspi}} = 9$ ) in step-and-stare mode		
Wavelengths (radiance)	450, 460, 470, 480, 490, 500, 510, 520, 530, 540, 550, 565, 580, 600, 670, and 750 nm ( $n_{\text{wave}}^{\text{spex}} = 16$ )	410, 469.1, 554.9, 670, and 863.4 nm ( $n_{\text{wave}}^{\text{rsp}} = 5$ )	355, 380, 445, 470, 555, 660, and 865 nm ( $n_{\text{wave}}^{\text{airmspi}} = 7$ )		
Wavelengths (polarization)	$\uparrow$	$\uparrow$	470, 660, and 865 nm		
Retrieved aerosol properties	Aerosol loading for each mode	$N^j, (j = 1, 2, \dots, n_{\text{mode}})$	$\leftarrow$	0.0001	$(\frac{0.25}{n_{\text{mode}}})^2$
	Fraction of spheres	$f_{\text{sphere}}^c$	$\leftarrow$	0.5	0.25
	Fine-mode component coefficient 1 (INORG)	$\alpha_1^f$	$\leftarrow$	0.95	$0.1^2$
	Fine-mode component coefficient 2 (BC)	$\alpha_2^f$	$\leftarrow$	0.005	$0.1^2$
	Coarse-mode component coefficient 1 (INORG)	$\alpha_1^c$	$\leftarrow$	0.95	$0.1^2$
	Coarse-mode component coefficient 2 (DUST)	$\alpha_2^c$	$\leftarrow$	0.005	$0.1^2$
Retrieved surface properties	Aerosol layer height (km)	ALH	$\leftarrow$	2.0	$4.0^2$
	BRDF scaling parameters for wavelength bands	$A(1, 2, \dots, n_{\text{wave}}^{\text{spex}})$	$A(1, 2, \dots, n_{\text{wave}}^{\text{rsp}})$	$A(1, 2, \dots, n_{\text{wave}}^{\text{airmspi}})$	0.0 $0.5^2$
	Parameter 1 of RPV model	$g$	$\leftarrow$	-0.09	$0.5^2$
	Parameter 2 of RPV model	$k$	$\leftarrow$	0.80	$0.5^2$
	Scaling parameter for polarized reflectance	$B$	$\leftarrow$	4.0	$2.0^2$

each variable in the state vector  $\mathbf{x}$ . Therefore, the optimization problem (Eq. 3) is reduced to

$$\tilde{\mathbf{x}}_{n+1} = \min_{\tilde{\mathbf{x}}} \left( \|\tilde{\mathbf{K}}(\tilde{\mathbf{x}} - \tilde{\mathbf{x}}_n) - \tilde{\mathbf{y}}\|^2 + \gamma^2 \|\tilde{\mathbf{x}} - \tilde{\mathbf{x}}_a\|^2 \right), \quad (5)$$

where  $\tilde{\mathbf{K}} = \mathbf{S}_y^{-\frac{1}{2}} \mathbf{K} \mathbf{W}^{\frac{1}{2}}$ ,  $\tilde{\mathbf{x}} = \mathbf{W}^{-\frac{1}{2}} \mathbf{x}$ , and  $\tilde{\mathbf{y}} = \mathbf{S}_y^{-\frac{1}{2}} (\mathbf{y} - \mathbf{F}(\mathbf{x}_n))$ .  $\mathbf{x}_a$  is the a priori state vector,  $\mathbf{W}$  is a weighting matrix that ensures that all state vector parameters range within the same order of magnitude (Hasekamp et al., 2011), and  $\mathbf{S}_y$  is the measurement error covariance matrix. Table 2 shows the values of  $\mathbf{x}_a$  for aerosol and surface

parameters.  $\mathbf{W}$  is a diagonal matrix, and its diagonal values are also shown in Table 2 (in the “weight” column). The solution of Eq. (5) is given by

$$\tilde{\mathbf{x}}_{n+1} = \tilde{\mathbf{x}}_n + \Lambda (\tilde{\mathbf{K}}^T \tilde{\mathbf{K}} + \gamma^2 \mathbf{I})^{-1} (\tilde{\mathbf{K}}^T \tilde{\mathbf{y}} - \gamma^2 (\tilde{\mathbf{x}}_n - \tilde{\mathbf{x}}_a)). \quad (6)$$

$\Lambda$  is a filtering–damping factor, which limits the step size for each iteration of the state vector. In this way, we use a Gauss–Newton scheme with reduced step size to avoid diverging retrievals (Hasekamp et al., 2011). The filter factor  $\Lambda$  values between 0 and 1. The regularization parameter  $\gamma^2$  in Eq. (3) is chosen optimally (for each iteration) from different

values (five values from 0.1 to 5) by evaluating the goodness of fit using a simplified (fast) forward model. In the SRON aerosol algorithm, the first guess is obtained before the full inversion retrieval using a multimode lookup table (LUT), which is based on tabulated RT calculations for each mode. The precalculated LUT is used as input for an approximate forward model in the LUT retrieval. Here, single-scattering is computed exactly as its computational cost is negligible. The fit parameters in the LUT retrieval are the aerosol column numbers for each mode and the surface parameters. For the first guess of the refractive index we use a fixed value of 1.45 for all modes. For further details we refer to Fu and Hasekamp (2018).

We use the goodness of fit ( $\chi^2$ ) to decide whether the retrievals have successfully converged:

$$\chi^2 = \frac{1}{n_{\text{meas}}} \sum_{i=1}^{n_{\text{meas}}} \frac{(F_i - y_i)^2}{S_y(i, i)}. \quad (7)$$

Here,  $n_{\text{meas}}$  is the total number of measurements (multi-angle and multispectral radiance and DoLP) for each pixel. We consider valid retrievals those that achieve a  $\chi^2$  smaller than an empirically chosen threshold  $\chi_{\text{max}}^2$ . This filter rejects cases in which the forward model is not able to fit the measurements, e.g., because of cloud-contaminated pixels (Stap et al., 2015, 2016) or corrupted measurements (Hasekamp et al., 2011), and cases in which the first-guess state vector deviates too much from the truth (Di Noia et al., 2015).

## 2.2 Fine-mode and coarse-mode effective radius

According to Eq. (2.53) in Hansen and Travis (1974), the effective radius is defined as follows:

$$r_{\text{eff}} = \frac{\int_{r_{\text{min}}}^{r_{\text{max}}} \pi r^3 n(r) dr}{\int_{r_{\text{min}}}^{r_{\text{max}}} \pi r^2 n(r) dr} = \frac{R}{O}, \quad (8)$$

where  $n(r)dr$  is the number of particles with a radius between  $r$  and  $r + dr$ ;  $r_{\text{min}}$  and  $r_{\text{max}}$  are the particle radius for the smallest and largest particles.

In this study, a five-mode retrieval is used. The effective radius for multiple modes together ( $r_{\text{eff}}^m$ ) is calculated from the different fixed modes by

$$r_{\text{eff}}^m = \frac{\sum_{i=1}^m R_i}{\sum_{i=1}^m O_i},$$

where  $n^m$  is the number of modes grouped together. For the five-mode retrievals in this study, we compute  $r_{\text{eff}}$  for the fine mode (modes 1–3 together) and coarse mode (modes 4 and 5 together).

## 2.3 Aerosol depolarization ratio and aerosol lidar ratio

The aerosol lidar properties are related to the aerosol scattering matrix. For some general assumptions, including (i) scattering by an assembly of randomly oriented particles each

having a plane of symmetry, (ii) scattering by an assembly containing particles and their mirror particles in equal numbers with random orientations, and (iii) Rayleigh scattering with or without depolarization effects, the aerosol scattering matrix has a simplified block-diagonal structure (Bottiger et al., 1980; Mishchenko, 2014):

$$\mathbf{F}(\Theta) = \begin{bmatrix} F_{11}(\Theta) & F_{12}(\Theta) & 0 & 0 \\ F_{12}(\Theta) & F_{22}(\Theta) & 0 & 0 \\ 0 & 0 & F_{33}(\Theta) & F_{34}(\Theta) \\ 0 & 0 & -F_{34}(\Theta) & F_{44}(\Theta) \end{bmatrix}, \quad (9)$$

where  $\Theta$  is the scattering angle and  $F_{11}$  is the phase function for total radiance.

The aerosol (linear) depolarization ratio is defined as

$$\delta_{\text{col}}^{\text{pol}} = \frac{F_{11}(180^\circ) - F_{22}(180^\circ)}{F_{11}(180^\circ) + F_{22}(180^\circ)}, \quad (10)$$

which is adapted from Eq. (3) in Mishchenko et al. (2016). We use Eq. (10) to compute an aerosol depolarization ratio from the aerosol properties of the MAPs and compare this to the vertically integrated value measured by HSRL-2, which is calculated by

$$\delta_{\text{col}}^{\text{hsrl}}(i) = \frac{\delta^{\text{hsrl}}(i)}{1 + \delta^{\text{hsrl}}(i)}, \quad \delta_{\text{col}}^{\text{hsrl}} = \frac{\sum_{i=0}^{n_{\text{bin}}} (\delta^{\text{hsrl}}(i) \beta_b^{\text{hsrl}}(i))}{\sum_{i=0}^{n_{\text{bin}}} (\beta_b^{\text{hsrl}}(i))},$$

$$\delta_{\text{col}}^{\text{hsrl}} = \frac{\hat{\delta}_{\text{col}}^{\text{hsrl}}}{1 - \hat{\delta}_{\text{col}}^{\text{hsrl}}}, \quad (11)$$

where  $i = 0$  corresponds to the bin closet to the surface, and  $i = n_{\text{bin}}$  corresponds to the bin closet to the aircraft. The aerosol backscatter coefficient ( $\beta_b^{\text{hsrl}}(i)$ ) for each bin is used as the weighting parameter.  $\delta^{\text{hsrl}}(i)$  is first transformed to  $\hat{\delta}^{\text{hsrl}}(i)$ , which is because  $\hat{\delta}^{\text{hsrl}}(i)$  mixes linearly like backscatter, but  $\delta^{\text{hsrl}}(i)$  does not (Burton et al., 2014).

In our retrieval algorithm we assume that for aerosols the single-scattering albedo  $\omega$  and  $F_{11}$  do not depend on altitude. In that case, using  $\omega$  and  $F_{11}(180^\circ)$ , we compute the vertically integrated aerosol extinction-to-backscatter ratio, i.e., the aerosol lidar ratio, for a MAP by

$$S_{\text{col}}^{\text{pol}} = \frac{4\pi}{\omega F_{11}(180^\circ)}, \quad (12)$$

which is adapted from Eq. (4) in Lopes et al. (2013). This can be compared to the corresponding value from HSRL-2:

$$S_{\text{col}}^{\text{hsrl}} = \frac{\sum_{i=0}^{n_{\text{bin}}} (\beta_e^{\text{hsrl}}(i))}{\sum_{i=0}^{n_{\text{bin}}} (\beta_b^{\text{hsrl}}(i))}, \quad (13)$$

which is adapted from Eq. (28) in Stamnes et al. (2018). Here  $\beta_e^{\text{hsrl}}(i)$  denotes the extinction coefficient for each bin.

### 3 Measurements

For this study, we use airborne measurements from three different polarimeters (SPEX airborne, RSP, AirMSPI) and one lidar (HSRL-2). Further, we use ground-based measurements for validation and reanalysis data as input to our retrieval algorithm. All data are described in this section.

#### 3.1 RSP

RSP (Cairns et al., 1999) started to operate on the NASA ER-2 in 2010 and has flown on a number of other airplanes since 2001 (Cairns et al., 2003). Multi-viewing capability over a large along-track angular range and at many viewing angles ( $\sim 150$ ) is obtained using a scanning mirror. Due to the fact that some viewing angles are blocked by the aircraft, the angular range of RSP on the ER-2 is restricted to  $-40$  to  $60^\circ$ . The Stokes parameters  $Q$  and  $U$  are analyzed in separate refractive telescopes using Wollaston prisms, followed by dichroic beam splitters. The RSP instrument is equipped with an in-flight calibration system, and the accuracy for the DoLP is better than 0.002 (Knobelspiesse et al., 2019), providing a benchmark (in DoLP) for other MAPs. Aerosol retrievals from RSP have been performed, amongst others, by Waquet et al. (2009), Wu et al. (2015), Wu et al. (2016), Di Noia et al. (2017), Stamnes et al. (2018), and Gao et al. (2019).

A complicating factor for using RSP measurements in aerosol retrievals over inhomogeneous land surfaces is that different viewing angles have different ground pixel size and may look at slightly shifted scenes on the ground. To partly overcome this problem we use (1) the approach of Wu et al. (2015) and construct RSP pixels that represent a 5 km along-track running average, as well as (2) the (moving average) approach of Di Noia et al. (2017) to select 10 viewing angles covering a broad viewing angle range (over the total RSP viewing angles), and convolve RSP measurements at each selected angle with an average of five angles. In this sense, although averaged measurements of 10 viewing angles are input to the retrieval algorithm, they are constructed from original RSP measurements at 50 angles. The viewing angles and wavelengths used in retrievals are summarized in Table 2. It should be noted that theoretically the shortwave infrared (SWIR) bands of RSP 1590 and 2250 nm would provide extra constraints for the characterization of coarse-mode aerosols. For the ACEPOL campaign, however, we found no improvement by including the SWIR bands and even slightly worse results (compared to AERONET and HSRL-2) in some cases. A possible explanation is that our assumption that the directional property of surface reflection is spectrally neutral does not hold over the full RSP wavelength range. Another explanation may be that the SWIR channels are affected by gas absorption, which we could not perfectly correct for.

#### 3.2 AirMSPI

AirMSPI (Diner et al., 2013) started to operate on the NASA ER-2 in October 2010. AirMSPI is an eight-band push-broom camera, which measures linear polarization in the 470, 660, and 865 nm bands. AirMSPI employs a photoelastic modulator-based polarimetric imaging technique to enable accurate measurements of the degree of linear polarization (DoLP) in addition to intensity. The instrument is mounted on a gimbal to acquire multi-angular observations in the range of  $\pm 67^\circ$ . AirMSPI has two principal observing modes: (1) step-and-stare, whereby  $11 \text{ km} \times 11 \text{ km}$  targets are observed at a discrete set of view angles with a spatial resolution of  $\sim 10 \text{ m}$ , and (2) continuous sweep, whereby the camera slews back and forth along the flight track at  $\pm 65^\circ$  to acquire wide area coverage ( $11 \text{ km}$  swath at nadir, target length  $108 \text{ km}$ ). The spatial resolution is  $\sim 25 \text{ m}$ . Aerosol retrievals from AirMSPI have been performed by Xu et al. (2017, 2018, 2019). In this study, only the step-and-stare measurements have been used as they provide a multi-angle view of the same ground scene. The nine viewing angles and seven wavelengths used in retrievals are summarized in Table 2. Following Xu et al. (2017), for AirMSPI we aggregate individual ground pixels to a  $1 \text{ km} \times 1 \text{ km}$  spatial grid in order to be less affected by surface inhomogeneity and its effect on the angular co-registration.

#### 3.3 SPEX airborne

SPEX airborne performed its first (engineering) flight on the ER-2 in 2016. ACEPOL was the first full science campaign. The instrument employs the spectral modulation technique (Snik et al., 2009) to accurately measure the degree of linear polarization (DoLP) in the spectral range 400–800 nm with a spectral resolution of 10–20 nm and the intensity at a higher spectral resolution of 2–3 nm. A ground-based version of SPEX has performed upward-looking measurements from the ground, which have been used to successfully retrieve aerosol microphysical and optical properties by van Harten et al. (2014) and Di Noia et al. (2015). For ACEPOL, Smit et al. (2019) performed a comparison between SPEX airborne and RSP for radiance and DoLP measurements at 410, 470, 550, and 670 nm. They found very good agreement between SPEX airborne and RSP at 550 and 670 nm, whereas the agreement gets worse towards smaller wavelengths. In this study, the nine viewing angles and 16 wavelengths used in retrievals are summarized in Table 2. The measurement at each wavelength represents an average of a 10 nm wide spectral region. We leave out the shortest wavelengths because of less good agreement with RSP and the wavelengths  $> 750 \text{ nm}$  because of order overlap of the grating. Each SPEX viewport has a moderate swath of  $\sim 6^\circ$  (Smit et al., 2019) in the across-track direction, which translates to a projected field of view from 2.4 km at nadir to 4.5 km at the fore and aft viewports when the instrument is operated at the typ-

ical altitude of ER-2. Conceptually, the instrument acts as nine separate push-broom spectrometers, which produce nine overlapping strips of data on the ground. In this way, a multi-angular view is obtained of ground scenes when the aircraft flies over it. The spatial sampling of the L1C product is chosen as  $1\text{ km} \times 1\text{ km}$  (across  $\times$  along-track), which is driven by the L1B spatial resolution of the outer viewports.

### 3.4 HSRL-2 data

The NASA Langley HSRL-2 instrument, operational since 2012, is a successor to the NASA Langley airborne HSRL-1 instrument, which was described by Hair et al. (2008) and Burton et al. (2012), then validated by Rogers et al. (2009). HSRL-2 uses the HSRL technique to independently measure aerosol extinction and backscatter at 355 nm (Burton et al., 2018) and 532 nm as well as the standard backscatter technique to measure aerosol backscatter at 1064 nm (Müller et al., 2014). It is polarization sensitive at all three wavelengths. HSRL-2 measures vertically resolved values for the backscatter coefficient ( $\beta$ ) and aerosol depolarization ratio at 355, 532, and 1064 nm (Burton et al., 2015) and the extinction coefficient and AOD at the high-spectral-resolution channels of 355 and 532 nm. HSRL-2 is the first airborne system capable of providing three backscatter and two extinction measurements, which is important for lidar retrievals of microphysical properties (Müller et al., 2014).

For the ACEPOL flights on the ER-2, the aerosol backscatter coefficient is derived using the HSRL technique at 355 and 532 nm, as well as the elastic backscatter technique at 1064 nm, and reported at a vertical resolution of 15 m and a horizontal and temporal resolution of 10 s (approximately 1–2 km at ER-2 cruise speeds). The aerosol depolarization ratios at all three wavelengths are reported at the same resolutions. For ACEPOL, the extinction products from the HSRL method are reported at 150 m vertical resolution and at a temporal resolution of 60 s generally as well as 10 s. Additionally, the aerosol extinction products at 355 and 532 nm are also provided based on the aerosol backscatter and an assumed lidar ratio of 40 sr; they are reported at the backscatter resolution.

Similarly, the AOD is reported from the standard HSRL approach, and the AOD calculated using the assumed lidar ratio is also provided. The reason why two AOD products are reported is that during ACEPOL, HSRL-2 experienced an interference that appears to be related to atmospheric turbulence. This interference impacted the ability to use the 532 and 355 nm molecular channels to derive aerosol extinction and AOD from the usual HSRL method. However, this interference did not impact the measurements of aerosol backscatter profiles, so these profiles were computed using the HSRL technique (i.e., the ratio of total backscatter to molecular backscatter). The systematic uncertainty on the AOD from the HSRL method is about 0.05 for ACEPOL, whereas the assumed lidar ratio produces systematic uncertainty that is

a constant relative fraction ( $\pm 50\%$ ). Therefore, for the case with high AOD (i.e., Figs. 7 and 8), the uncertainty is smaller when using the HSRL method, and we therefore use these products for this case. Conversely, although the uncertainties are fairly high for both products for low AOD, the product using an assumed lidar ratio is expected to have lower uncertainties, and we use these products for the low AOD cases (i.e., Figs. 4, 5, and 6) in this paper.

### 3.5 AERONET data

The multispectral aerosol optical depth (AOD) from the MAP and lidar retrievals is validated with AERONET (AErosol RObotic NETwork) level 1.5 data (Holben et al., 2001) (version 3.0). The data are cloud cleared. The uncertainty on AERONET AOD is 0.01 for mid-visible wavelengths and 0.03 for UV wavelengths (Eck et al., 1999); it is dominated by a calibration (systematic) error. The effective radii for fine and coarse modes are compared with AERONET level 1.5 Almucantar Retrieval Inversion Products (Dubovik et al., 2002). The AODs of fine and coarse modes are compared with AERONET level 1.5 spectral deconvolution algorithm (SDA) data (O'Neill et al., 2003). It should be noted that the inversion and SDA products are quite uncertain themselves at low AOD, so the comparison to these products should not be considered a validation. In this paper, data from the following six AERONET stations are used for validation: Bakersfield, CalTech, Flagstaff (USGS\_Flagstaff\_ROLO), Fresno\_2, Modesto, and Railroad Valley.

### 3.6 Reanalysis data

The required meteorological inputs for our retrieval scheme are vertical profiles of humidity, temperature, and pressure. We obtain this information from National Centers for Environmental Prediction (NCEP) reanalysis data (Kalnay et al., 1996). For ozone absorption in retrievals, we use the ozone profiles from the Modern-Era Retrospective analysis for Research and Applications version 2 (MERRA-2) (Gelaro et al., 2017). The  $\text{NO}_2$  columns are taken from Air Force Geophysics Laboratory (AFGL) database. The data are interpolated to the specific time and location of a MAP ground pixel.

## 4 Results

We apply the SRON algorithm as described in Sect. 2.1 to measurements of SPEX, RSP, and AirMSPI. In our retrievals we use an ad hoc representation of the measurement error covariance matrix  $\mathbf{S}_y$ , whereby we assume a diagonal matrix for  $\mathbf{S}_y$  (i.e., errors are uncorrelated for different wavelengths and viewing angles) with values on the diagonal corresponding to 5 % error on the radiance and 0.005 on DoLP. Although this is a crude assumption that does not reflect a bottom-up estimate taking into account individual error sources, it should



be noted that for the chosen inversion approach the most important aspect is the relative dependence between radiance and DoLP errors because we include a flexible regularization parameter that is determined as part of the retrieval. The same results can be obtained when assuming 2.5 % radiance and 0.0025 DoLP errors, in combination with a different  $\chi^2$  filter. This relative dependence between radiance and DoLP accuracies seems reasonable for all three instruments given that they all have a high DoLP accuracy. Another note is that there are error sources, such as misregistration between different viewing angles, that are not included in an uncertainty model (as they are not directly related to pure instrument performance) but that are significant and possibly even dominant over land.

To compare MAP retrievals with AERONET or HSRL-2,  $\chi^2 < 1.5$  is used in this paper (for SPEX, RSP, and AirMSPI) as the filter for the goodness of fit. We also apply filters on the number of viewing angles ( $\geq 9$ ), the smallest scattering angle ( $< 120^\circ$ ), and the largest scattering angle ( $> 120^\circ$ ). To evaluate the retrieved aerosol properties, four measures are used, which are the mean absolute error (MAE), the mean relative error (MRE), the bias, and the standard deviation (SD). Two types of plots are included in this paper for comparisons. One is the scatter plot with the  $x$  and  $y$  axis for two instruments. The other one is the Bland–Altman (Bland and Altman, 1986) plot (difference plot), wherein the differences between two instruments are plotted against the averages of the two instruments.

#### 4.1 SPEX airborne, RSP, and AirMSPI versus AERONET

We first compare the polarimetric (SPEX, RSP, and AirMSPI) retrievals with the AERONET data for the aerosol optical depth (AOD) at three wavelengths: 380, 440, and 675 nm. For the comparison, retrievals within 10 km around each AERONET station are selected and averaged. The AERONET data are averaged within 1 h around the time of the ER-2 overpass. The results of the AOD comparison are shown in Fig. 1, where panels a and d correspond to SPEX airborne, panels b and e to RSP, and panels c and f to AirMSPI. The 12 overpasses between SPEX and AERONET are consistent with those between RSP and AERONET, i.e., one averaged value from SPEX (Fig. 1a) and RSP (Fig. 1b) corresponds to the same averaged value from AERONET. For AirMSPI (Fig. 1c), eight overpasses are consistent with SPEX and RSP, while the other four comparison points do not have corresponding points for SPEX and RSP. The reason for this inconsistency in comparison points is that AirMSPI was not making measurements for some of the AERONET overpasses. On the other hand, some of the SPEX and RSP overpasses are screened out because there were no ground pixels with enough colocated viewing angles because of aircraft yaw, while the swath of AirMSPI is sufficiently large to still get colocated angles despite the yaw.

For the AOD at 440 nm, the MAE is respectively 0.016, 0.024, and 0.014, the MRE is respectively 0.175, 0.289, and 0.139, the bias is respectively 0.003,  $-0.010$ , and  $-0.004$ , and the SD is respectively 0.019, 0.027, and 0.017 for SPEX, RSP, and AirMSPI. The MAE, bias, and SD are within 0.01 and the MRE is within 0.15 for the instruments, whereas the values for SPEX airborne and AirMSPI are somewhat smaller than for RSP. Similar conclusions hold for the AOD at 380 or 675 nm. For each instrument, the MAE gets smaller with increasing wavelengths, which is mainly caused by the fact that the AOD value itself decreases with wavelength. Based on the comparisons above, we can conclude that SPEX, RSP, and AirMSPI all achieve good agreement with AERONET and the differences in performance between the instruments are small.

For the comparison of the fine- and coarse-mode effective radius ( $r_{\text{eff}}^f$  and  $r_{\text{eff}}^c$ ), it should be noted that it is difficult to retrieve them when AOD is small. Therefore, shown in Fig. 2 is the comparison when  $\tau_{380}$  is larger than 0.1. The remaining cases are still very challenging but we would lose too many points if we further increase the AOD limit. The solid lines shown in the plot are bias  $\pm$  SD. The retrievals of  $r_{\text{eff}}^f$  compared with AERONET are shown in Fig. 2a–c, where the MAE is 0.022, 0.021, and 0.028  $\mu\text{m}$  for SPEX, RSP, and AirMSPI, respectively. SPEX and RSP compare somewhat better in terms of MAE and bias, whereas AirMSPI has a small SD. However, overall the differences between the instruments are small and the number of comparison points is very limited, which means that differences between instruments can be explained by one or two points. The  $r_{\text{eff}}^c$  comparisons corresponding to SPEX, RSP, and AirMSPI are shown in Fig. 2d–f, respectively. All three instruments have a poor comparison with AERONET for  $r_{\text{eff}}^c$ , with an MAE close to 1.5  $\mu\text{m}$ . This is in line with synthetic studies (e.g., Hasekamp et al., 2019a) showing that  $r_{\text{eff}}^c$  is a difficult parameter to retrieve, in particular for small AOD values. It should be noted that AERONET consistently gives a larger coarse-mode effective radius than MAPs. A possible explanation is that the effective radius for the coarse modes 4 and 5 in our five-mode retrieval is 0.882 and 1.719, respectively (see Table 1); thus, the coarse-mode effective radius from MAPs calculated based on Eq. (8) is estimated and limited between 0.882 and 1.719, whereas AERONET gives values between 2.25 and 3.3 (when  $\tau_{380}$  is larger than 0.1). A comparable range is expected for MAPs if a parametric two-mode retrieval or a seven-mode retrieval (Fu and Hasekamp, 2018) is used. Also, it should be noted that “fine” and “coarse” as defined by the almucantar retrievals are different than defining fine and coarse by specific modes as shown in Table 1. This may introduce differences in the comparisons.

For the comparison of the fine- and coarse-mode AOD ( $\tau^f$  and  $\tau^c$ ), the results are shown in Fig. 3. The comparison shows an MAE of 0.028, 0.029, and 0.012 for SPEX, RSP, and AirMSPI, respectively, for  $\tau^f$  and 0.026, 0.028, and 0.017 for  $\tau^c$ . The bias is 0.028, 0.019, and 0.004 for

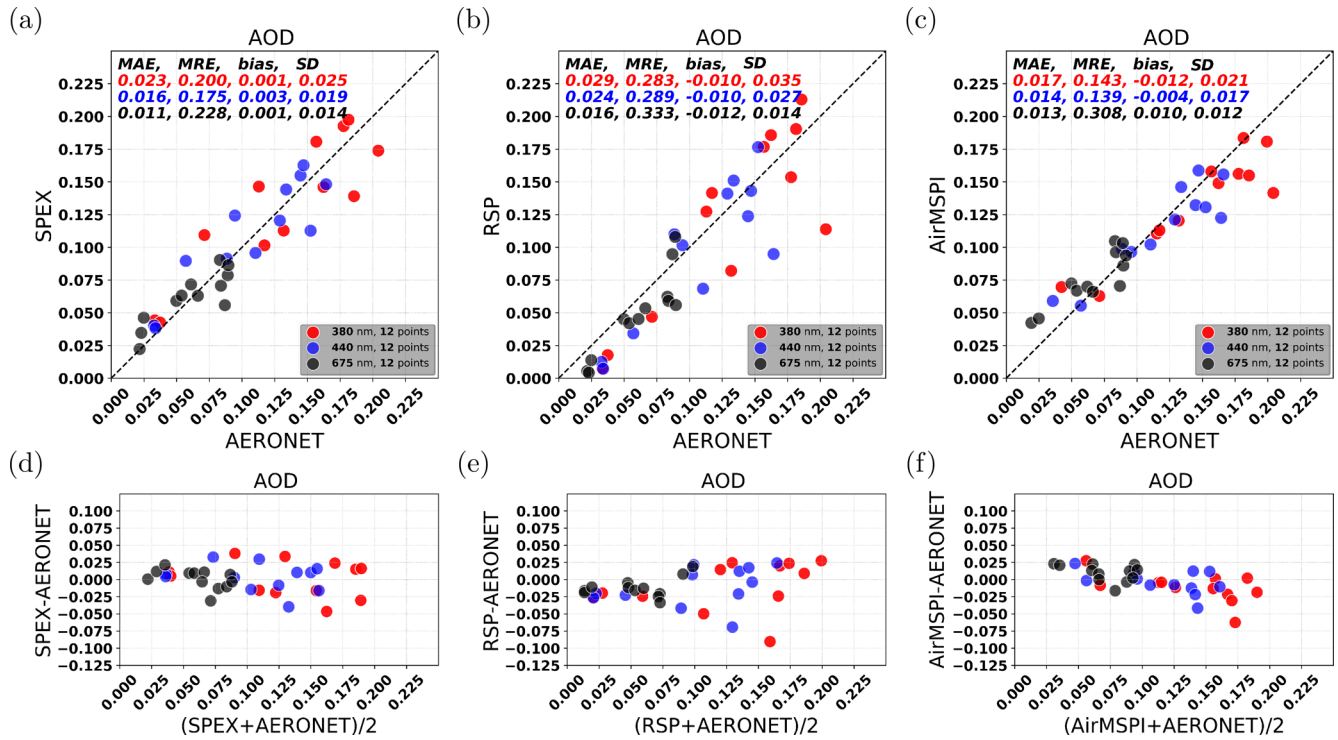


**Figure 1.** Comparison with AERONET for AOD (380, 440, and 675 nm) among SPEX, RSP, and AirMSPI retrievals. (a, b, c) SPEX, RSP, and AirMSPI comparison with AERONET, respectively. (d, e, f) Bland–Altman plots (or difference plots) between SPEX and AERONET, between RSP and AERONET, and between AirMSPI and AERONET, respectively.

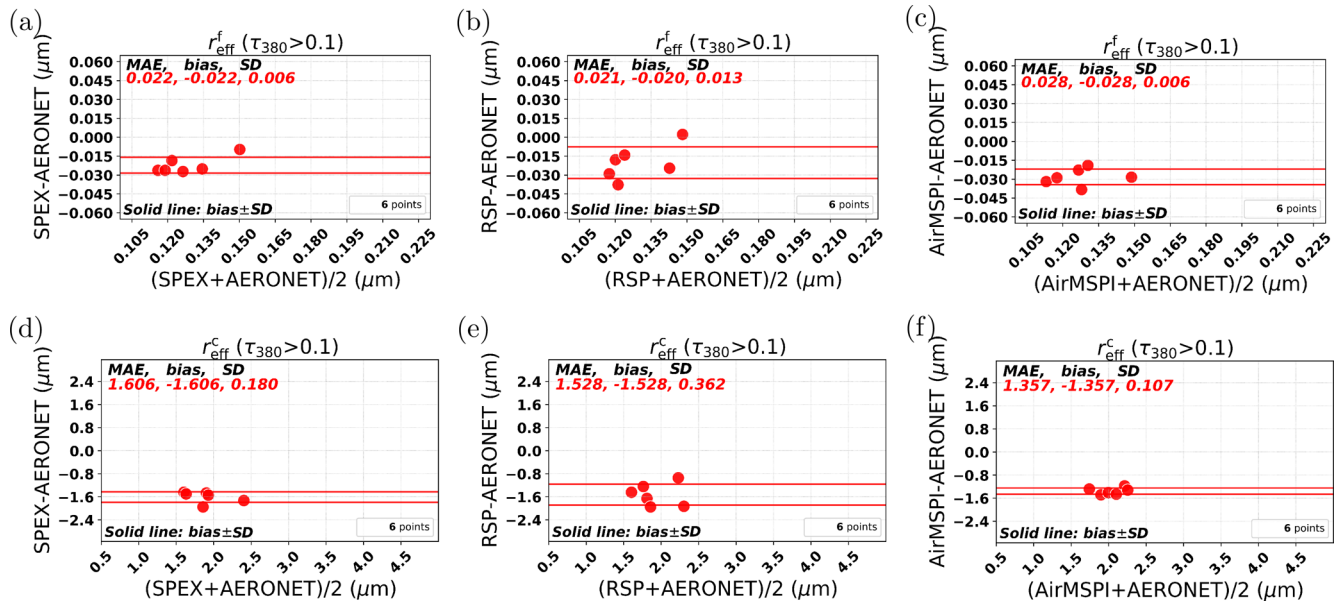


**Figure 2.** Comparison with AERONET for the effective radius of the fine and coarse modes ( $r_{\text{eff}}^f$  and  $r_{\text{eff}}^c$ ) among SPEX, RSP, and AirMSPI retrievals. (a, b, c) Bland–Altman plots for  $r_{\text{eff}}^f$  between SPEX and AERONET, between RSP and AERONET, and between AirMSPI and AERONET, respectively. (d, e, f) Bland–Altman plots for  $r_{\text{eff}}^c$  between SPEX and AERONET, between RSP and AERONET, and between AirMSPI and AERONET, respectively.

$\tau^f$  and 0.025, 0.028, and 0.003 for  $\tau^c$ . So, SPEX and RSP have an overestimation of the fine mode and an underestimation of the coarse mode compared to the AERONET SDA product. Although these biases are large in a relative sense (given the low AOD, especially for the coarse mode), they are within the expected error from the AERONET SDA product. AirMSPI compares better to the AERONET SDA product than SPEX airborne and RSP. Again, it should be noted that the AirMSPI comparison does not contain exactly the same points as the comparison for SPEX and RSP. It should also be noted that for RSP, since no SWIR channels are included in the retrieval to nail the coarse mode, we do not expect it to do well in retrieving coarse-mode properties. It is important to note that for the low AOD values encountered during ACEPOL, the AERONET-retrieved fine- and coarse-mode AOD and effective radius are very uncertain themselves. Therefore, this comparison should not be interpreted as “retrieval versus truth” but rather as “retrieval versus retrieval”.

## 4.2 Comparison between SPEX airborne, RSP, and HSRL-2

For the comparison to HSRL-2, we only use SPEX airborne and RSP because these provided a continuous data stream during ACEPOL, while AirMSPI only provides step-and-stare measurements for specific targets.

### 4.2.1 Comparison HSRL-2 to AERONET

Given that we use HSRL-2 as a reference for our MAP retrievals, it is important to first validate HSRL-2 with AERONET. Figure 4 shows the comparison of the HSRL-2 AOD at 355 and 532 nm with AERONET (log–log interpolated between 340 and 380 nm for 355 nm and between 500 and 675 nm for 532 nm). From the comparison it follows that the HSRL-2 AOD at 532 nm agrees very well with AERONET, with a small MAE (0.012), a small MRE (0.269), a small absolute bias (0.005), and a small SD (0.014). The comparison at 355 nm is somewhat worse than that at 532 nm with an MAE of 0.028, an MRE of 0.357, a bias of  $-0.014$ , and an SD of 0.029. The bias between HSRL-2 and AERONET is within the AERONET uncertainty. The random differences, with standard deviation 0.029 at 380 nm and 0.014 at 532 nm, are most likely due to HSRL-2 uncertainties. Note that shown in Fig. 4 are the points corresponding to the days 23 October, 25 October, 26 October, and 7 November 2017.

### 4.2.2 Low AOD case on 26 October 2017

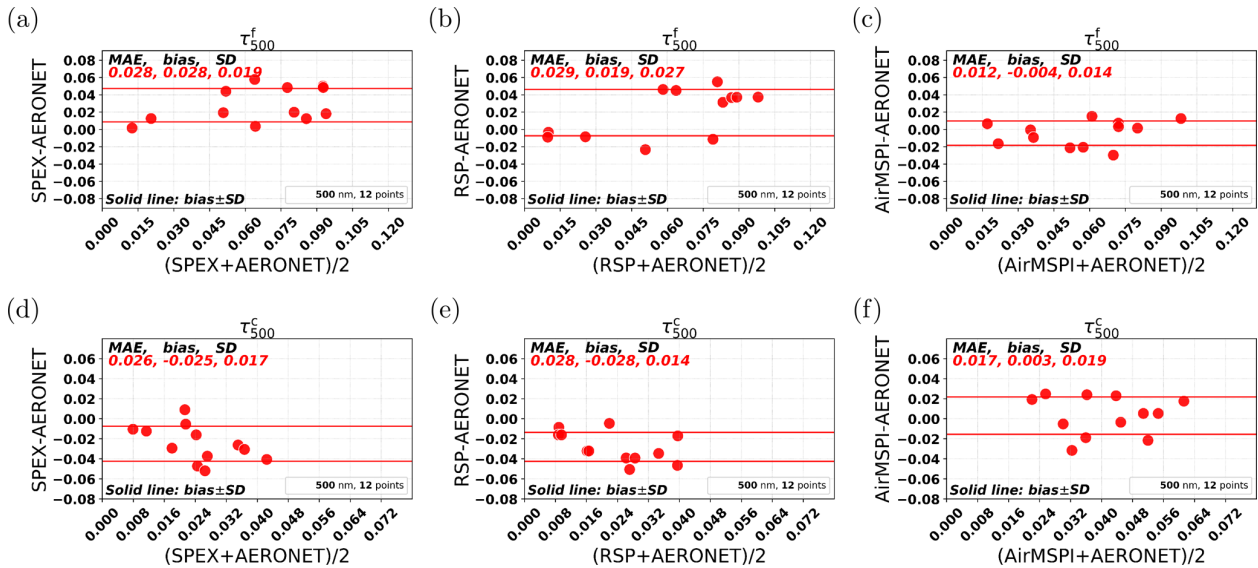
In this subsection, we compare the aerosol properties from SPEX and RSP with those from HSRL-2 for 26 October 2017 with low aerosol loading (AOD at 532 nm in the range 0.02 to 0.14). The results for AOD at 355 and 532 nm are shown in Fig. 5. Figure 5a shows the retrieved AOD from HSRL-2 for the ground pixels colocated with SPEX and RSP. From this

figure it follows that there were very low AOD values for the eastern part of the scene and somewhat higher values in the western and southwestern part of the scene. Figure 5b shows the AOD comparison between SPEX and HSRL-2 with the MAE 0.014, the MRE 0.296, the bias 0.009, and the SD 0.018 at 532 nm, as well as the MAE 0.028, the MRE 0.321, the bias  $-0.006$ , and the SD 0.034 at 355 nm. Figure 5c shows the AOD comparison between RSP and HSRL-2 with the MAE 0.022, the MRE 0.418, the bias  $-0.007$ , and the SD 0.028 at 532 nm, as well as the MAE 0.037, the MRE 0.369, the bias  $-0.008$ , and the SD 0.048 at 355 nm. So, SPEX shows a very good agreement with HSRL-2 for this challenging scene of low AOD over land with a relatively bright surface. SPEX compares somewhat better to HSRL-2 than RSP for this case at both 532 and 355 nm. The Bland–Altman plots Fig. 5e and f show a larger scatter and more outliers for RSP. A possible explanation is that for low AOD the radiance and polarization measurements have a strong influence from the spatially inhomogeneous surface, and therefore errors due to inter-angle misregistration, which are larger for RSP than for SPEX, may be significant. For these cases there is larger sensitivity to spatial mismatch between different viewing angles, and RSP, as a single-pixel-swath instrument, is more sensitive to such mismatches. Figure 5d shows the AOD comparison between SPEX and RSP with the MAE 0.024, the MRE 0.831, the bias 0.016, and the SD 0.025. The differences from the direct comparison between SPEX and RSP are somewhat larger than those from individual comparisons of HSRL-2 with SPEX and RSP. This suggests that the differences with HSRL-2 are not caused by common assumptions in the SPEX and RSP retrievals but are rather caused by errors that are specific to each MAP.

For the retrieved surface parameters, we do not have a good reference to evaluate the accuracy. Instead, Fig. 6 shows the AOD difference between MAP and HSRL-2 as a function of the retrieved BRDF scaling parameter  $A$ , for which we do not see clear correlation or dependence.

### 4.2.3 High AOD on 9 November 2017

In this subsection, polarimetric retrievals from SPEX airborne and RSP are compared to HSRL-2 on 9 November 2017 for a smoke plume with high AOD (including AOD values  $> 1.0$ ). Figure 7a shows the original AOD (i.e., no filter or colocation included) from SPEX for the flight leg over the smoke plume. This gives a sense of how variable the smoke plume is. Figure 7b shows the AOD comparison between SPEX and HSRL-2, for which the MAE is 0.088, the MRE is 0.693, the bias is  $-0.029$ , and the SD is 0.149 at 532 nm. Figure 7c shows the AOD comparison between RSP and HSRL-2, for which the MAE is 0.079, the MRE is 0.564, the bias is  $-0.024$ , and the SD is 0.142 at 532 nm. Figure 7d shows the AOD comparison between SPEX and RSP, for which the MAE is 0.044, the MRE is 0.155, the bias is  $-0.005$ , and the SD is 0.063 at 532 nm. RSP compares



**Figure 3.** Comparison with AERONET for the AOD of the fine and coarse modes ( $\tau_{500}^f$  and  $\tau_{500}^c$ ) among SPEX, RSP, and AirMSPI retrievals. (a, b, c) Bland–Altman plots for  $\tau_{500}^f$  between SPEX and AERONET, between RSP and AERONET, and between AirMSPI and AERONET, respectively. (d, e, f) Bland–Altman plots for  $\tau_{500}^c$  between SPEX and AERONET, between RSP and AERONET, and between AirMSPI and AERONET, respectively.

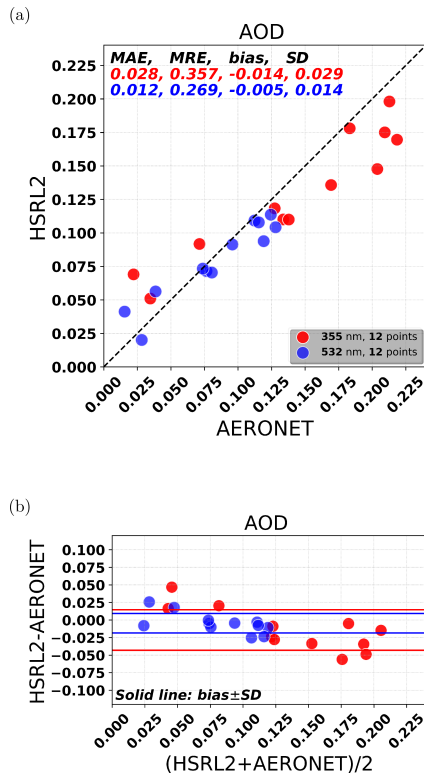


**Figure 4.** Comparison between HSRL-2 and AERONET for AOD at 355 and 532 nm. (a, b) The scatter plot and the difference plot, respectively.

slightly better to HSRL-2 than SPEX with respect to MAE and MRE. It should be noted that the smoke plume exhibits large spatial variation, so part of the MAP–lidar differences can be attributed to the fact that different instruments see a slightly different part of the smoke plume. Furthermore, both SPEX and RSP show a similar negative bias in AOD at both 355 and 532 nm, as well as one clear outlier point in the comparison with HSRL-2 at the highest AOD. This is also clear from the corresponding Bland–Altman plots in Fig. 7e and f. Given the very similar underestimation in both SPEX and RSP (compared to HSRL-2) and the good comparison between SPEX and RSP, it is unlikely that this underestimation is caused by aspects related to instrumental errors of the two different MAPs. It might be possible that the underestimation is related to the MAP retrieval approach, which is the same for both instruments, but based on earlier studies with real and synthetic measurements we have no indication for this. Another possibility is that HSRL-2 overestimates the AOD at this high aerosol loading or the large spatial variability has a larger effect on the MAP–lidar comparison than on the inter-MAP comparison. At high AOD the performance of RSP is more similar to that of SPEX than for low AOD. Our explanation for this is that at high AOD the measured radiance and DoLP are less affected by the co-registration errors between viewing angles than for low AOD.

For the high AOD case, we also compare the aerosol depolarization ratio ( $\delta$ ) and aerosol lidar ratio ( $S$ ) from SPEX and RSP with HSRL-2. Figure 8a–c respectively show the comparison of the aerosol depolarization ratio between SPEX and HSRL-2, between RSP and HSRL-2, and between SPEX and

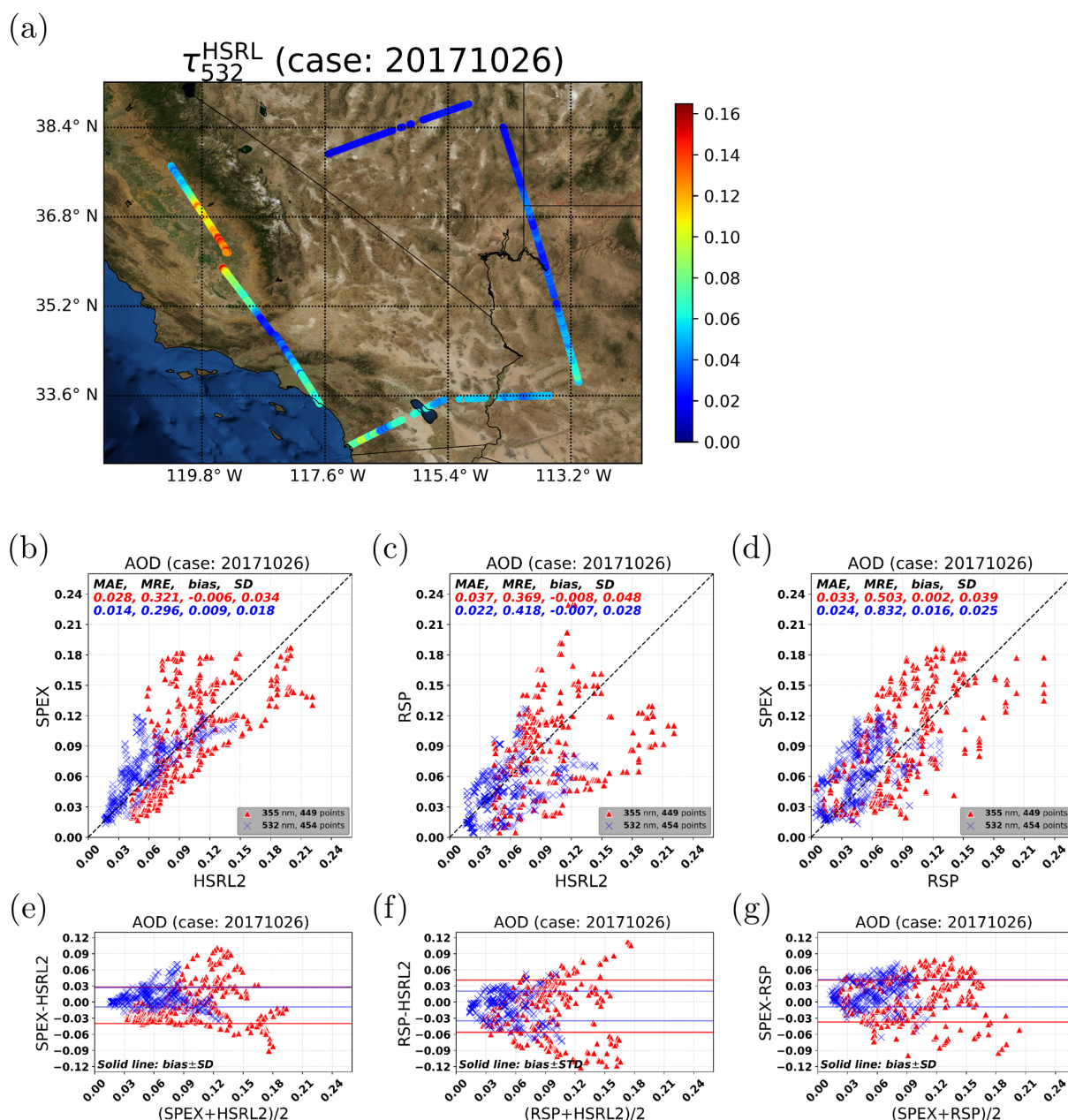


**Figure 5.** Comparison with HSRL-2 from 26 October 2017 (low AOD case) for AOD (355 and 532 nm) between SPEX and RSP retrievals. (a) HSRL-2 AOD collocation with SPEX and RSP. (The map is generated using Python's basemap package and its ArcGIS image service ESRI\_Imagery\_World\_2D.) (b) SPEX AOD comparison with HSRL-2. (c) RSP AOD comparison with HSRL-2. (d) SPEX AOD comparison with RSP. (e, f, g) Bland–Altman plots for (b, c, d), respectively.

RSP. It can be observed that both SPEX and RSP show a similar behavior against HSRL-2, especially at 355 nm: there is an underestimation towards lower values of the depolarization ratio, but, on the other hand, there is a reasonable agreement with HSRL-2 for both instruments. Again, given the fact that the performance of both SPEX and RSP versus HSRL-2 is very similar, we conclude that the main reason for the difference between SPEX/RSP and HSRL-2 does not

lie in instrumental errors for the MAPs. A possible explanation for the difference could be the simplified description of nonspherical particles in our retrieval approach. On the other hand, the overall comparison of the aerosol depolarization ratio with HSRL-2 confirms the capability of both SPEX and RSP to retrieve information on particle shape. The results of the aerosol lidar ratio are shown in Fig. 8d–f. Both SPEX and RSP show a similar overestimation of the lidar



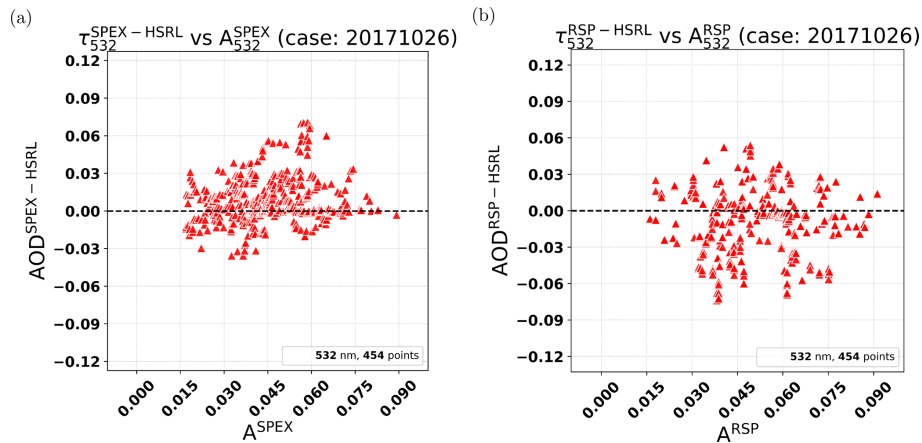


**Figure 6.** The AOD difference between MAP and HSRL-2 as a function of the retrieved BRDF scaling parameter  $A$  at 532 nm. **(a)** AOD difference between SPEX and HSRL-2 versus  $A$ . **(b)** AOD difference between RSP and HSRL-2 versus  $A$ .

ratio compared to HSRL-2, and SPEX and RSP agree quite well. Again, it is unlikely that the overestimation is related to instrumental errors in the MAPs. Overall, the agreement with HSRL-2 for the aerosol lidar ratio is reasonable for both SPEX and RSP.

#### 4.2.4 Median and standard deviation properties of the smoke plume

The median and standard deviation properties for the smoke plume as measured by SPEX and RSP are summarized in Table 3. Here, we only include retrievals for which AOD > 0.2 at 532 nm because for those cases the accurate retrieval of microphysical properties is expected (e.g., Hasekamp et al., 2019a). The number of points to calculate the median and the standard deviation is the same for SPEX and RSP. Also, we only include fine-mode microphysical properties because there is only a very small coarse-mode contribution to the smoke plume. SPEX and RSP compare well for the fine-mode refractive index, fine-mode effective radius, fine- and coarse-mode AOD, and SSA (relative to requirements as formulated, e.g., by Mishchenko et al., 2004). Reasonable agreement is found for the fraction of spherical particles. For the aerosol layer height (ALH), SPEX retrieves a higher value (4.417 km) than RSP (1.148 km), and the latter value is somewhat closer to the ALH derived from HSRL-2 (2.64 km). Here, it should be noted that for SPEX the shortest wavelength used in the retrieval is 450 nm, so we do not expect an accurate ALH retrieval because the retrieval of ALH from polarization requires a strong signal from Rayleigh scattering (Wu et al., 2016). Figure 9 shows the number particle size distribution from SPEX and RSP in the smoke plume, which confirms that the smoke plume is fine-mode dominated.

The values of the aerosol properties in Table 3 (for both SPEX and RSP) are in the range that is expected for smoke. First of all, it is expected that smoke is dominated by fine

particles (e.g., Russell et al., 2014), which is confirmed by the much larger retrieved fine-mode AOD than coarse-mode AOD by both MAPs. The real part of the refractive index is consistent with the study of Levin et al. (2010) for the Fire Laboratory at Missoula Experiment (FLAME), who found mostly refractive indices for biomass burning between 1.55 and 1.60. Also, the SSA values in Table 3 are representative for fresh biomass burning smoke. For example, Nicolae et al. (2013) found SSA values of 0.79 at 532 nm for smoke with an age of 0.25 d and 0.93 for smoke with an age of 0.75 d. Both the values retrieved by SPEX and RSP can be considered realistic for smoke.

## 5 Discussions and conclusions

In this study, we performed aerosol retrievals from different MAPs employed during the ACEPOL campaign and evaluated them against ground-based AERONET measurements and against HSRL-2 measurements. The polarimetric aerosol retrievals were performed using the SRON algorithm in a multimode setup (Fu and Hasekamp, 2018) on SPEX airborne, RSP (without SWIR channels), and AirMSPI.

For the AERONET comparison, only scenes with low AOD (0.03–0.17 at 440 nm) were available during ACEPOL. For these scenes, SPEX, RSP, and AirMSPI all show good agreement with AERONET for AOD (MAE 0.016, 0.024, and 0.014 for AOD at 440 nm). For the fine-mode effective radius, we found MAEs with AERONET of 0.022, 0.021, and 0.028 for SPEX, RSP, and AirMSPI, respectively. For the effective radius comparison we only compare scenes with AOD > 0.10 at 380 nm, but it should be noted that the remaining cases are still very challenging and that the difference in performance between the different instruments are caused by just one or two comparison points. All three instruments had a poor comparison with AERONET for the coarse-mode effective radius. This was because the coarse-

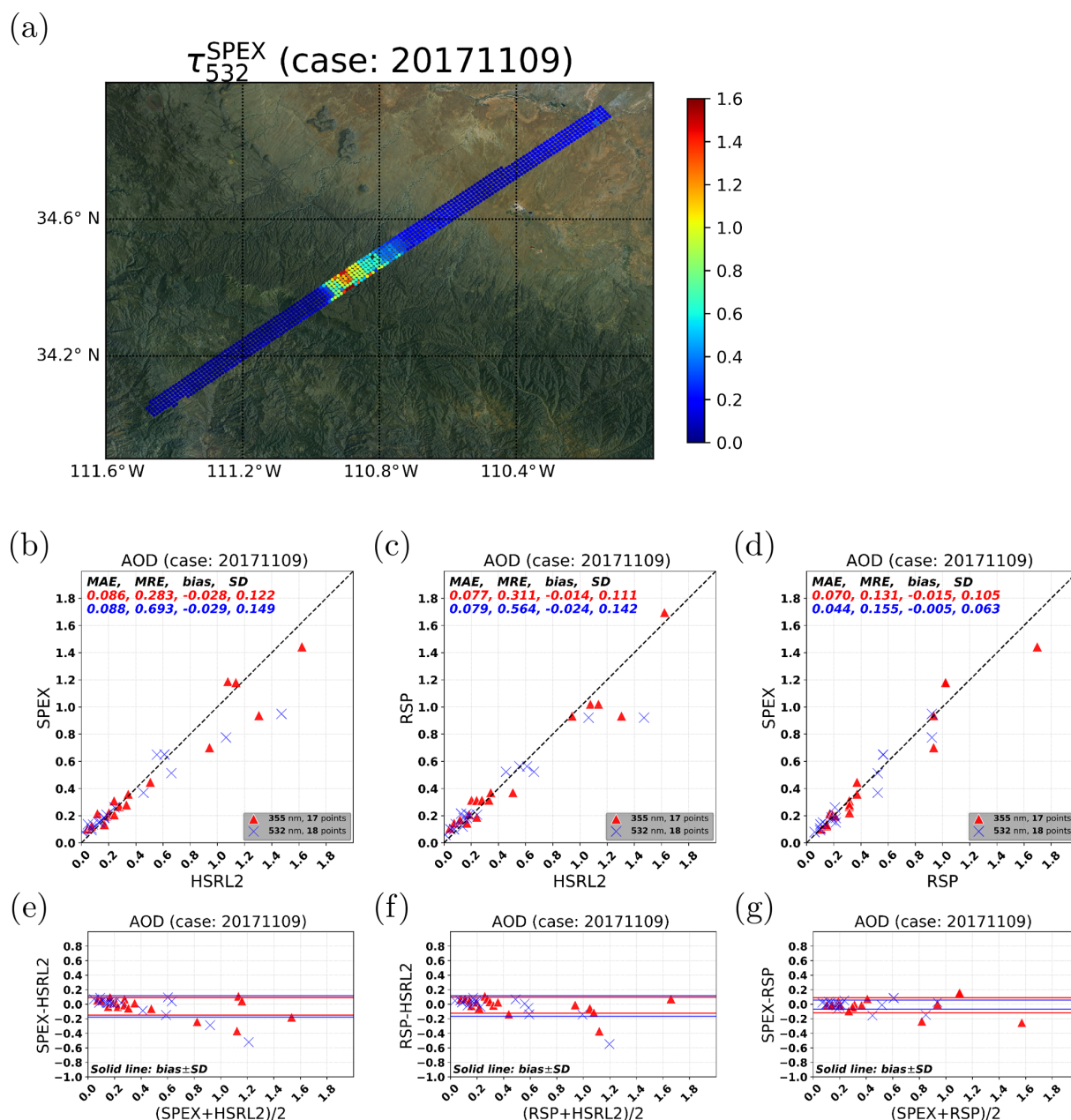


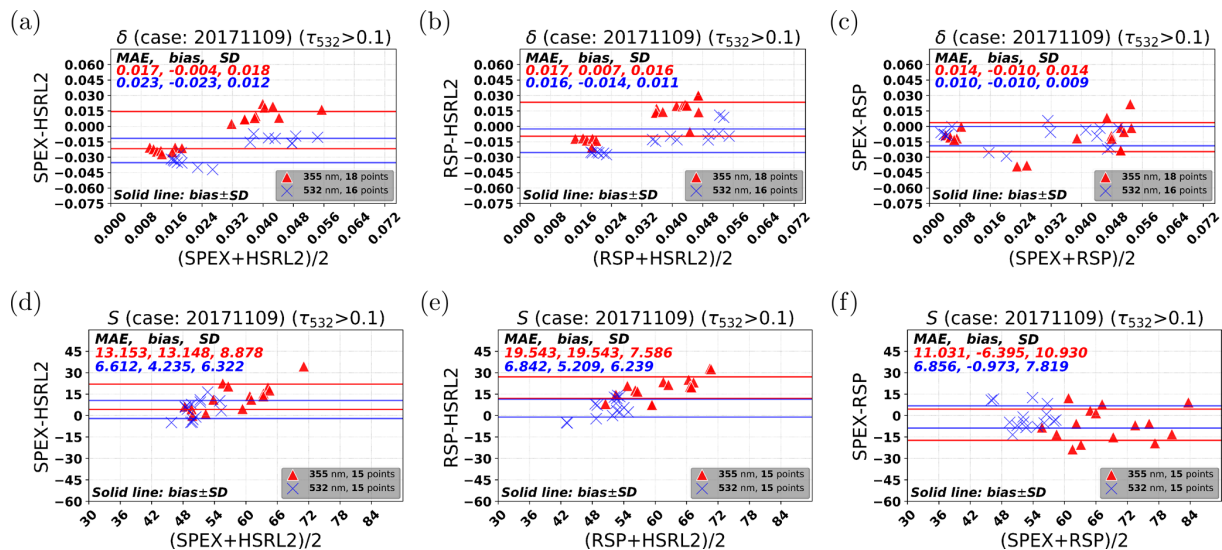
**Figure 7.** Comparison with HSRL-2 from 9 November 2017 (high AOD smoke case) for AOD (355 and 532 nm) between SPEX and RSP retrievals. (a) SPEX original AOD, i.e., no filter or colocation included. (The map is generated using Python's basemap package and its ArcGIS image service ESRI\_Imagery\_World\_2D.) (b) SPEX AOD comparison with HSRL-2. (c) RSP AOD comparison with HSRL-2. (d) SPEX AOD comparison with RSP. (e, f, g) Bland–Altman plots for (b, c, d), respectively.

mode effective radius was a difficult parameter to retrieve, in particular for small AOD values. For the fine-mode AOD, good agreements with AERONET were shown for all three MAPs, with a somewhat better performance for AirMSPI. For the coarse-mode AOD, SPEX and RSP show reasonable agreement, while AirMSPI also shows good agreement here. It should be noted, however, that the comparison for AirMSPI is not based on exactly the same points as for SPEX and RSP.

For the comparison between the MAPs (SPEX and RSP) and HSRL-2, we focused on a day with low AOD and a flight leg with high AOD (including measurements with AOD > 1.0) over a prescribed forest fire in Arizona (9 November). For the challenging case of low AOD over land, it was shown that SPEX and RSP are capable of providing accurate retrievals of AOD. For this low AOD case, SPEX showed a better comparison against HSRL-2 than RSP.

**Table 3.** Median and standard deviation (SD) properties of the smoke plume from SPEX and RSP when AOD > 0.2 at 532 nm.

	SPEX		RSP	
	Median	SD	Median	SD
Fine-mode real part of refractive index ( $m_{r,532}^f$ )	1.579	0.019	1.556	0.059
Fine-mode imaginary part of refractive index ( $m_{i,532}^f$ )	0.038	0.011	0.036	0.013
Fine-mode effective radius ( $r_{\text{eff}}^f$ )	0.116	0.004	0.119	0.007
Fine-mode AOD ( $\tau_{532}^f$ )	0.554	0.238	0.509	0.231
Coarse-mode AOD ( $\tau_{532}^c$ )	0.016	0.011	0.040	0.029
Aerosol layer height (ALH) (km)	4.417	1.148	1.585	1.588
SSA ( $\omega_{532}$ )	0.815	0.044	0.829	0.044
Fraction of spherical particles ( $f_{\text{sphere}}$ )	0.989	0.149	0.846	0.133

**Figure 8.** Comparison with HSRL-2 from 9 November 2017 (high AOD smoke case) for the aerosol depolarization ratio ( $\delta$ ) and the aerosol lidar ratio ( $S$ ) between SPEX and RSP retrievals. (a) SPEX  $\delta$  comparison with HSRL-2. (b) RSP  $\delta$  comparison with HSRL-2. (c) SPEX  $\delta$  comparison with RSP. (d) SPEX  $S$  comparison with HSRL-2. (e) RSP  $S$  comparison with HSRL-2. (f) SPEX  $S$  comparison with RSP.

For the retrievals over the smoke plume a reasonable agreement in AOD between the MAPs and HSRL-2 was also found, despite the fact that the comparison was hampered by large spatial variability in AOD throughout the smoke plume. In addition, a good agreement was found between the MAPs (SPEX, RSP) and HSRL-2 for the aerosol depolarization ratio, which indicates that the MAPs are capable of retrieving particle sphericity. A reasonable comparison was also found for the aerosol lidar ratio.

For the ALH SPEX retrieved a value that was high (by  $\sim 1.5$  km) compared to HSRL-2, while the ALH retrieved from RSP agreed somewhat better with HSRL-2, although it was  $\sim 1$  km lower. Here, it should be noted that we do not expect a good ALH retrieval from SPEX airborne because the shortest wavelength used in the retrieval was 450 nm. For the retrieved microphysical and optical properties of the smoke plume, SPEX and RSP agreed very well with each other, and

both instruments retrieved smoke properties that were in line with earlier studies.

In this study, three polarimeters produced comparable results when using the same algorithm. The exceptions were the ALH and some coarse-mode parameters, which were mainly caused by not having the bands that these parameters were sensitive to: shortwave (410 nm) and SWIR, respectively. For parameters that the instruments were sensitive to, good agreements were found among instruments. Our results corroborate the findings of earlier studies that different combinations of spectral and angular measurements yield a very similar retrieval capability for aerosol properties (Hasekamp and Landgraf, 2007; Wu et al., 2015; Hasekamp et al., 2019a)

**Data availability.** The ACEPOL data from MAPs and lidars can be downloaded from the following website: <https://www-air.larc.nasa.gov/cgi-bin/ArcView/acepol> (last access: 22 January 2020; NASA,



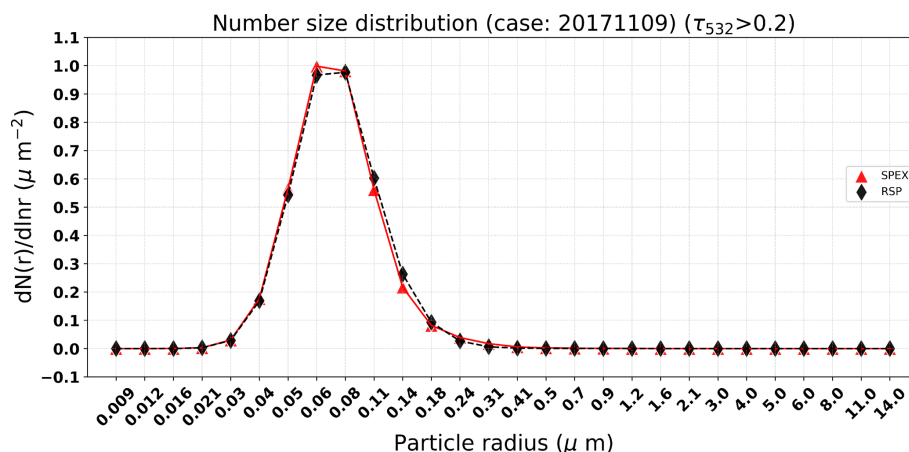


**Figure 9.** Number particle size distribution in the smoke plume retrieved from SPEX and RSP.

2020) (registration required). The AERONET data can be downloaded from the following website: <https://aeronet.gsfc.nasa.gov/> (last access: 22 January 2020). The meteorological NCEP data can be accessed through the following website: <http://www.cdc.noaa.gov/> (last access: 22 January 2020). The polarimetric retrieval results will be made available on SRON's ftp site.

**Author contributions.** GF and OH designed and performed the research; JR, MS, and ADN took care of operations and calibration processing of SPEX airborne, BC and AW of RSP, DD of airMSPI, and SB, CH, JH, and RF of HSRL2. FX and MG provided input for independent evaluation of the retrievals. FS, KK, AdS, RF, and OH contributed to the campaign definition and flight planning. GF and OH wrote the paper. All authors contributed to the improvement of the paper by providing comments and suggestions.

**Competing interests.** The authors declare that they have no conflict of interest.

**Acknowledgements.** This work is funded by the NWO/NSO project ACEPOL (Aerosol Characterization from Polarimeter and Lidar) under project number ALW-GO/16-09. We thank all the members involved in the ACEPOL campaign. We acknowledge the former Aerosol, Cloud, Ecosystem (ACE) program at NASA's Earth Science Division as a sponsor for ACEPOL flights. We thank the field teams making measurements on the ground as some of those were critical to the measurement accuracy (i.e., vicarious calibration). We also acknowledge the support received by the ground and air crew at NASA AFRC in Palmdale. Part of this research was carried out at the Jet Propulsion Laboratory, California Institute of Technology, under a contract with the National Aeronautics and Space Administration (80NM0018D004). We thank the AERONET team and the MERRA-2 team for maintaining the data. NCEP Reanalysis data were provided by the NOAA/OAR/ESRL PSD, Boulder, Colorado, USA, from their website at <https://www.esrl.noaa.gov/psd/> (last access: 22 January 2020). We would also like to thank the Netherlands Supercomputing Centre (SURFsara) for providing us with the

computing facility, the Cartesius cluster. We are very grateful to the editor, Lorraine Remer, two other reviewers, and Sergey Korkin for their reviews and insightful comments.

**Financial support.** This research has been supported by the Netherlands Organisation for Scientific Research (NWO)/the Netherlands Space Office (NSO) Aerosol Characterization from Polarimeter and Lidar (ACEPOL) (project no. ALW-GO/16-09) and the Jet Propulsion Laboratory, California Institute of Technology (National Aeronautics and Space Administration (contract no. 80NM0018D004)).

**Review statement.** This paper was edited by Jun Wang and reviewed by Lorraine Remer and two anonymous referees.

## References

- Bland, J. M. and Altman, D.: STATISTICAL METHODS FOR ASSESSING AGREEMENT BETWEEN TWO METHODS OF CLINICAL MEASUREMENT, *The Lancet*, 327, 307–310, [https://doi.org/10.1016/S0140-6736\(86\)90837-8](https://doi.org/10.1016/S0140-6736(86)90837-8), 1986.
- Böttger, J. R., Fry, E. S., and Thompson, R. C.: Phase Matrix Measurements for Electromagnetic Scattering by Sphere Aggregates, in: *Light Scattering by Irregularly Shaped Particles*, edited by: Schuerman, D. W., Springer US, Boston, MA, 283–290, [https://doi.org/10.1007/978-1-4684-3704-1\\_33](https://doi.org/10.1007/978-1-4684-3704-1_33), 1980.
- Bucholtz, A.: Rayleigh-scattering calculations for the terrestrial atmosphere, *Appl. Optics*, 34, 2765–2773, <https://doi.org/10.1364/AO.34.002765>, 1995.
- Burton, S. P., Ferrare, R. A., Hostetler, C. A., Hair, J. W., Rogers, R. R., Obland, M. D., Butler, C. F., Cook, A. L., Harper, D. B., and Froyd, K. D.: Aerosol classification using airborne High Spectral Resolution Lidar measurements – methodology and examples, *Atmos. Meas. Tech.*, 5, 73–98, <https://doi.org/10.5194/amt-5-73-2012>, 2012.
- Burton, S. P., Vaughan, M. A., Ferrare, R. A., and Hostetler, C. A.: Separating mixtures of aerosol types in airborne High Spec-

- tral Resolution Lidar data, *Atmos. Meas. Tech.*, 7, 419–436, <https://doi.org/10.5194/amt-7-419-2014>, 2014.
- Burton, S. P., Hair, J. W., Kahnert, M., Ferrare, R. A., Hostetler, C. A., Cook, A. L., Harper, D. B., Berkoff, T. A., Seaman, S. T., Collins, J. E., Fenn, M. A., and Rogers, R. R.: Observations of the spectral dependence of linear particle depolarization ratio of aerosols using NASA Langley airborne High Spectral Resolution Lidar, *Atmos. Chem. Phys.*, 15, 13453–13473, <https://doi.org/10.5194/acp-15-13453-2015>, 2015.
- Burton, S. P., Hostetler, C. A., Cook, A. L., Hair, J. W., Seaman, S. T., Scola, S., Harper, D. B., Smith, J. A., Fenn, M. A., Ferrare, R. A., Saide, P. E., Chemyakin, E. V., and Müller, D.: Calibration of a high spectral resolution lidar using a Michelson interferometer, with data examples from ORACLES, *Appl. Optics*, 57, 6061–6075, <https://doi.org/10.1364/AO.57.006061>, 2018.
- Cairns, B., Russell, E. E., and Travis, L. D.: Research Scanning Polarimeter: calibration and ground-based measurements, in: *Proc. SPIE 3754, Polarization: Measurement, Analysis, and Remote Sensing II*, 25 October 1999, edited by: Goldstein, D. H. and Chenault, D. B., SPIE, 186–197, <https://doi.org/10.1117/12.366329>, 1999.
- Cairns, B., Russell, E. E., LaVeigne, J. D., and Tennant, P. M. W.: Research scanning polarimeter and airborne usage for remote sensing of aerosols, in: *Proc. SPIE 5158, Polarization Science and Remote Sensing*, edited by: Shaw, J. A. and Tyo, J. S., SPIE, 33–44, <https://doi.org/10.1117/12.518320>, 2003.
- Cairns, B., LaVeigne, J. D., Rael, A., and Granneman, R. D.: Atmospheric correction of HyperSpecTIR measurements using the research scanning polarimeter, in: *Proc. SPIE 5158, Polarization Science and Remote Sensing*, edited by: Goldstein, D. H. and Chenault, D. B., SPIE, 95–105, <https://doi.org/10.1117/12.542194>, 2004.
- Chen, C., Dubovik, O., Henze, D. K., Lapyonok, T., Chin, M., Ducos, F., Litvinov, P., Huang, X., and Li, L.: Retrieval of desert dust and carbonaceous aerosol emissions over Africa from POLDER/PARASOL products generated by the GRASP algorithm, *Atmos. Chem. Phys.*, 18, 12551–12580, <https://doi.org/10.5194/acp-18-12551-2018>, 2018.
- Chowdhary, J., Cairns, B., Mishchenko, M. I., Hobbs, P. V., Cota, G. F., Redemann, J., Rutledge, K., Holben, B. N., and Russell, E.: Retrieval of Aerosol Scattering and Absorption Properties from Photopolarimetric Observations over the Ocean during the CLAMS Experiment, *J. Atmos. Sci.*, 62, 1093–1117, <https://doi.org/10.1175/JAS3389.1>, 2005.
- D’Almeida, G. A., Koepke, P., and Shettle, E. P.: *Atmospheric Aerosols: Global Climatology and Radiative Characteristics*, A Deepak Pub, Hampton, 1991.
- Deschamps, P., Breon, F., Leroy, M., Podaire, A., Bricaud, A., Buriez, J., and Seze, G.: The POLDER mission: instrument characteristics and scientific objectives, *IEEE T. Geosci. Remote*, 32, 598–615, <https://doi.org/10.1109/36.297978>, 1994.
- Deuzé, J. L., Goloub, P., Herman, M., Marchand, A., Perry, G., Susana, S., and Tanré, D.: Estimate of the aerosol properties over the ocean with POLDER, *J. Geophys. Res.*, 105, 15329–15346, 2000.
- Deuzé, J. L., Goloub, P., Herman, M., Marchand, A., Perry, G., Susana, S., and Tanré, D.: Estimate of the aerosol properties over the ocean with POLDER, *J. Geophys. Res.*, 105, 15329–15346, <https://doi.org/10.1029/2000jd900148>, 2000.
- Deuzé, J. L., Bréon, F. M., Devaux, C., Goloub, P., Herman, M., Lafrance, B., Maignan, F., Marchand, A., Nadal, F., Perry, G., and Tanré, D.: Remote sensing of aerosols over land surfaces from POLDER-ADEOS-1 polarized measurements, *J. Geophys. Res.*, 106, 4913–4926, <https://doi.org/10.1029/2000jd900364>, 2001.
- Diner, D. J., Xu, F., Garay, M. J., Martonchik, J. V., Rheingans, B. E., Geier, S., Davis, A., Hancock, B. R., Jovanovic, V. M., Bull, M. A., Capraro, K., Chipman, R. A., and McClain, S. C.: The Airborne Multiangle Spectropolarimetric Imager (AirMSPI): a new tool for aerosol and cloud remote sensing, *Atmos. Meas. Tech.*, 6, 2007–2025, <https://doi.org/10.5194/amt-6-2007-2013>, 2013.
- Diner, D. J., Boland, S. W., Brauer, M., Bruegge, C., Burke, K. A., Chipman, R., Girolamo, L. D., Garay, M. J., Hasheminassab, S., Hyer, E., Jerrett, M., Jovanovic, V., Kalashnikova, O. V., Liu, Y., Lyapustin, A. I., Martin, R. V., Nastan, A., Ostro, B. D., Ritz, B., Schwartz, J., Wang, J., and Xu, F.: Advances in multiangle satellite remote sensing of speciated airborne particulate matter and association with adverse health effects: from MISR to MAIA, *J. Appl. Remote Sens.*, 12, 042603, <https://doi.org/10.1117/1.JRS.12.042603>, 2018.
- Di Noia, A., Hasekamp, O. P., van Harten, G., Rietjens, J. H. H., Smit, J. M., Snik, F., Henzing, J. S., de Boer, J., Keller, C. U., and Volten, H.: Use of neural networks in ground-based aerosol retrievals from multi-angle spectropolarimetric observations, *Atmos. Meas. Tech.*, 8, 281–299, <https://doi.org/10.5194/amt-8-281-2015>, 2015.
- Di Noia, A., Hasekamp, O. P., Wu, L., van Diedenhoven, B., Cairns, B., and Yorks, J. E.: Combined neural network/Phillips–Tikhonov approach to aerosol retrievals over land from the NASA Research Scanning Polarimeter, *Atmos. Meas. Tech.*, 10, 4235–4252, <https://doi.org/10.5194/amt-10-4235-2017>, 2017.
- Dubovik, O., Holben, B. N., Lapyonok, T., Sinyuk, A., Mishchenko, M. I., Yang, P., and Slutsker, I.: Non-spherical aerosol retrieval method employing light scattering by spheroids, *Geophys. Res. Lett.*, 29, 54-1–54-4, <https://doi.org/10.1029/2001gl014506>, 2002.
- Dubovik, O., Sinyuk, A., Lapyonok, T., Holben, B. N., Mishchenko, M., Yang, P., Eck, T. F., Volten, H., Muñoz, O., Veihelmann, B., van der Zande, W. J., Leon, J. F., Sorokin, M., and Slutsker, I.: Application of spheroid models to account for aerosol particle nonsphericity in remote sensing of desert dust, *J. Geophys. Res.*, 111, D11208, <https://doi.org/10.1029/2005jd006619>, 2006.
- Dubovik, O., Herman, M., Holdak, A., Lapyonok, T., Tanré, D., Deuzé, J. L., Ducos, F., Sinyuk, A., and Lopatin, A.: Statistically optimized inversion algorithm for enhanced retrieval of aerosol properties from spectral multi-angle polarimetric satellite observations, *Atmos. Meas. Tech.*, 4, 975–1018, <https://doi.org/10.5194/amt-4-975-2011>, 2011.
- Dubovik, O., Li, Z., Mishchenko, M. I., Tanré, D., Karol, Y., Bojkov, B., Cairns, B., Diner, D. J., Espinosa, W. R., Goloub, P., Gu, X., Hasekamp, O., Hong, J., Hou, W., Knobelspiesse, K. D., Landgraf, J., Li, L., Litvinov, P., Liu, Y., Lopatin, A., Marbach, T., Maring, H., Martins, V., Meijer, Y., Milinevsky, G., Mukai, S., Parol, F., Qiao, Y., Remer, L., Rietjens, J., Sano, I., Stammes, P., Stammes, S., Sun, X., Tabary, P., Travis, L. D., Waquet, F., Xu, F., Yan, C., and Yin, D.: Polarimetric remote sensing of atmospheric

- aerosols: Instruments, methodologies, results, and perspectives, *J. Quant. Spectrosc. Ra.*, 224, 474–511, 2019.
- Eck, T. F., Holben, B. N., Reid, J. S., Dubovik, O., Smirnov, A., O'Neill, N. T., Slutsker, I., and Kinne, S.: Wavelength dependence of the optical depth of biomass burning, urban, and desert dust aerosols, *J. Geophys. Res.*, 104, 31333–31349, <https://doi.org/10.1029/1999JD900923>, 1999.
- Fan, C., Fu, G., Di Noia, A., Smit, M., H. H. Rietjens, J., A. Ferrare, R., Burton, S., Li, Z., and P. Hasekamp, O.: Use of A Neural Network-Based Ocean Body Radiative Transfer Model for Aerosol Retrievals from Multi-Angle Polarimetric Measurements, *Remote Sensing*, 11, 2877, <https://doi.org/10.3390/rs11232877>, 2019.
- Fougnie, B., Marbach, T., Lacan, A., Lang, R., Schlüssel, P., Poli, G., Munro, R., and Couto, A. B.: The multi-viewing multi-channel multi-polarisation imager – Overview of the 3MI polarimetric mission for aerosol and cloud characterization, *J. Quant. Spectrosc. Ra.*, 219, 23–32, <https://doi.org/10.1016/j.jqsrt.2018.07.008>, 2018.
- Fu, G. and Hasekamp, O.: Retrieval of aerosol microphysical and optical properties over land using a multimode approach, *Atmos. Meas. Tech.*, 11, 6627–6650, <https://doi.org/10.5194/amt-11-6627-2018>, 2018.
- Gao, M., Zhai, P.-W., Franz, B. A., Hu, Y., Knobelspiesse, K., Werdell, P. J., Ibrahim, A., Cairns, B., and Chase, A.: Inversion of multiangular polarimetric measurements over open and coastal ocean waters: a joint retrieval algorithm for aerosol and water-leaving radiance properties, *Atmos. Meas. Tech.*, 12, 3921–3941, <https://doi.org/10.5194/amt-12-3921-2019>, 2019.
- Gelaro, R., McCarty, W., Suárez, M. J., Todling, R., Molod, A., Takacs, L., Randles, C. A., Darmenov, A., Bosilovich, M. G., Reichle, R., Wargan, K., Coy, L., Cullather, R., Draper, C., Akella, S., Buchard, V., Conaty, A., da Silva, A. M., Gu, W., Kim, G.-K., Koster, R., Lucchesi, R., Merkova, D., Nielsen, J. E., Parityka, G., Pawson, S., Putman, W., Rienecker, M., Schubert, S. D., Sienkiewicz, M., and Zhao, B.: The Modern-Era Retrospective Analysis for Research and Applications, Version 2 (MERRA-2), *J. Climate*, 30, 5419–5454, <https://doi.org/10.1175/JCLI-D-16-0758.1>, 2017.
- Hair, J. W., Hostetler, C. A., Cook, A. L., Harper, D. B., Ferrare, R. A., Mack, T. L., Welch, W., Izquierdo, L. R., and Hovis, F. E.: Airborne High Spectral Resolution Lidar for profiling aerosol optical properties, *Appl. Optics*, 47, 6734–6752, <https://doi.org/10.1364/AO.47.006734>, 2008.
- Hansen, J. E. and Travis, L. D.: Light scattering in planetary atmospheres, *Space Sci. Rev.*, 16, 527–610, <https://doi.org/10.1007/BF00168069>, 1974.
- Hasekamp, O. P.: Capability of multi-viewing-angle photopolarimetric measurements for the simultaneous retrieval of aerosol and cloud properties, *Atmos. Meas. Tech.*, 3, 839–851, <https://doi.org/10.5194/amt-3-839-2010>, 2010.
- Hasekamp, O. P. and Landgraf, J.: A linearized vector radiative transfer model for atmospheric trace gas retrieval, *J. Quant. Spectrosc. Ra.*, 5, 221–238, [https://doi.org/10.1016/s0022-4073\(01\)00247-3](https://doi.org/10.1016/s0022-4073(01)00247-3), 2002.
- Hasekamp, O. P. and Landgraf, J.: Retrieval of aerosol properties over the ocean from multispectral single-viewing-angle measurements of intensity and polarization: Retrieval approach, information content, and sensitivity study, *J. Geophys. Res.*, 110, D20207, <https://doi.org/10.1029/2005jd006212>, 2005.
- Hasekamp, O. P. and Landgraf, J.: Retrieval of aerosol properties over land surfaces: capabilities of multiple-viewing-angle intensity and polarization measurements, *Appl. Optics*, 46, 3332–3344, <https://doi.org/10.1364/AO.46.003332>, 2007.
- Hasekamp, O. P., Litvinov, P., and Butz, A.: Aerosol properties over the ocean from PARASOL multiangle photopolarimetric measurements, *J. Geophys. Res.*, 116, D14204, <https://doi.org/10.1029/2010JD015469>, 2011a.
- Hasekamp, O. P., Fu, G., Rusli, S. P., Wu, L., Di Noia, A., van de Brugh, J., Landgraf, J., Martijn Smit, J., Rietjens, J., and van Amerongen, A.: Aerosol measurements by SPeXone on the NASA PACE mission: expected retrieval capabilities, *J. Quant. Spectrosc. Ra.*, 227, 170–184, <https://doi.org/10.1016/j.jqsrt.2019.02.006>, 2019a.
- Hasekamp, O. P., Gryspeerdt, E., and Quaas, J.: Analysis of polarimetric satellite measurements suggests stronger cooling due to aerosol-cloud interactions, *Nat. Commun.*, 10, 1–7, <https://doi.org/10.1038/s41467-019-13372-2>, 2019b.
- Herman, M., Deuzé, J. L., Devaux, C., Goloub, P., Bréon, F. M., and Tanré, D.: Remote sensing of aerosols over land surfaces including polarization measurements and application to POLDER measurements, *J. Geophys. Res.*, 102, 17039–17049, <https://doi.org/10.1029/96jd02109>, 1997.
- Hill, S. C., Hill, A. C., and Barber, P. W.: Light scattering by size/shape distributions of soil particles and spheroids, *Appl. Optics*, 23, 1025–1031, <https://doi.org/10.1364/AO.23.001025>, 1984.
- Holben, B. N., Tanré, D., Smirnov, A., Eck, T. F., Slutsker, I., Abuhassan, N., Newcomb, W. W., Schafer, J. S., Chatenet, B., Lavenu, F., Kaufman, Y. J., Castle, J. V., Setzer, A., Markham, B., Clark, D., Frouin, R., Halthore, R., Karneli, A., O'Neill, N. T., Pietras, C., Pinker, R. T., Voss, K., and Zibordi, G.: An emerging ground-based aerosol climatology: Aerosol optical depth from AERONET, *J. Geophys. Res.*, 106, 12067–12097, <https://doi.org/10.1029/2001jd900014>, 2001.
- Illingworth, A. J., Barker, H. W., Beljaars, A., Ceccaldi, M., Chepfer, H., Clerbaux, N., Cole, J., Delanoë, J., Domenech, C., Donovan, D. P., Fukuda, S., Hiraoka, M., Hogan, R. J., Huenerbein, A., Kollias, P., Kubota, T., Nakajima, T., Nakajima, T. Y., Nishizawa, T., Ohno, Y., Okamoto, H., Oki, R., Sato, K., Satoh, M., Shephard, M. W., Velázquez-Blázquez, A., Wandinger, U., Wehr, T., and van Zadelhoff, G.-J.: The Earth-CARE Satellite: The Next Step Forward in Global Measurements of Clouds, Aerosols, Precipitation, and Radiation, *B. Am. Meteorol. Soc.*, 96, 1311–1332, <https://doi.org/10.1175/BAMS-D-12-00227.1>, 2014.
- IPCC: Climate Change 2014: Synthesis Report. Contribution of Working Groups I, II and III to the Fifth Assessment Report of the Intergovernmental Panel on Climate Change, edited by: Core Writing Team, Pachauri, R. K., and Meyer, L. A., IPCC, Geneva, Switzerland, Tech. rep. AR5, available at: <https://www.ipcc.ch/report/ar5/syr/> (last access: 22 January 2020), 2014.
- Kalnay, E., Kanamitsu, M., Kistler, R., Collins, W., Deaven, D., Gandin, L., Iredell, M., Saha, S., White, G., Woollen, J., Zhu, Y., Leetmaa, A., Reynolds, B., Chelliah, M., Ebisuzaki, W., Higgins, W., Janowiak, J., Mo, K. C., Ropelewski, C., Wang, J., Jenne, R., and Joseph, D.:

- The NCEP/NCAR 40-Year Reanalysis Project, *B. Am. Meteorol. Soc.*, 77, 437–472, [https://doi.org/10.1175/1520-0477\(1996\)077<0437:TNYRP>2.0.CO;2](https://doi.org/10.1175/1520-0477(1996)077<0437:TNYRP>2.0.CO;2), 1996.
- Kaufman, Y. and Tanre, D.: Atmospherically resistant vegetation index (ARVI) for EOS-MODIS, *IEEE T. Geosci. Remote*, 30, 261–270, <https://doi.org/10.1109/36.134076>, 1992.
- Knobelspiesse, K., Cairns, B., Mishchenko, M., Chowdhary, J., Tsigaridis, K., van Dienenhoven, B., Martin, W., Ottaviani, M., and Alexandrov, M.: Analysis of fine-mode aerosol retrieval capabilities by different passive remote sensing instrument designs, *Opt. Express*, 20, 21457–21484, 2012.
- Knobelspiesse, K., Tan, Q., Bruegge, C., Cairns, B., Chowdhary, J., Dienenhoven, B. v., Diner, D., Ferrare, R., Harten, G. v., Jovanovic, V., Ottaviani, M., Redemann, J., Seidel, F., and Sinclair, K.: Intercomparison of airborne multi-angle polarimeter observations from the Polarimeter Definition Experiment, *Appl. Optics*, 58, 650–669, <https://doi.org/10.1364/AO.58.000650>, 2019.
- Lacagnina, C., Hasekamp, O. P., Bian, H., Curci, G., Myhre, G., van Noije, T., Schulz, M., Skeie, R. B., Takemura, T., and Zhang, K.: Aerosol single-scattering albedo over the global oceans: Comparing PARASOL retrievals with AERONET, OMI, and AeroCom models estimates, *J. Geophys. Res.-Atmos.*, 120, 9814–9836, <https://doi.org/10.1002/2015jd023501>, 2015.
- Lacagnina, C., Hasekamp, O. P., and Torres, O.: Direct radiative effect of aerosols based on PARASOL and OMI satellite observations, *J. Geophys. Res.-Atmos.*, 122, 2366–2388, <https://doi.org/10.1002/2016jd025706>, 2017.
- Landgraf, J., Hasekamp, O. P., Box, M. A., and Trautmann, T.: A linearized radiative transfer model for ozone profile retrieval using the analytical forward-adjoint perturbation theory approach, *J. Geophys. Res.*, 106, 27291–27305, <https://doi.org/10.1029/2001JD000636>, 2001.
- Levin, E. J. T., McMeeking, G. R., Carrico, C. M., Mack, L. E., Kreidenweis, S. M., Wold, C. E., Moosmüller, H., Arnott, W. P., Hao, W. M., Collett, J. L., and Malm, W. C.: Biomass burning smoke aerosol properties measured during Fire Laboratory at Missoula Experiments (FLAME), *J. Geophys. Res.*, 115, D18210, <https://doi.org/10.1029/2009JD013601>, 2010.
- Litvinov, P., Hasekamp, O., and Cairns, B.: Models for surface reflection of radiance and polarized radiance: Comparison with airborne multi-angle photopolarimetric measurements and implications for modeling top-of-atmosphere measurements, *Remote Sens. Environ.*, 115, 781–792, <https://doi.org/10.1016/j.rse.2010.11.005>, 2011.
- Lopes, F. J. S., Landulfo, E., and Vaughan, M. A.: Evaluating CALIPSO's 532 nm lidar ratio selection algorithm using AERONET sun photometers in Brazil, *Atmos. Meas. Tech.*, 6, 3281–3299, <https://doi.org/10.5194/amt-6-3281-2013>, 2013.
- Maignan, F., Bréon, F.-M., Fédèle, E., and Bouvier, M.: Polarized reflectances of natural surfaces: Spaceborne measurements and analytical modeling, *Remote Sens. Environ.*, 113, 2642–2650, <https://doi.org/10.1016/j.rse.2009.07.022>, 2009.
- Martins, J. V., Fernandez-Borda, R., McBride, B., Remer, L., and Barbosa, H. M. J.: The Harp Hyperangular Imaging Polarimeter and the Need for Small Satellite Payloads with High Science Payoff for Earth Science Remote Sensing, in: *IGARSS 2018 – 2018 IEEE International Geoscience and Remote Sensing Symposium*, Valencia, Spain, 22–27 July 2018, IEEE, 6304–6307, <https://doi.org/10.1109/IGARSS.2018.8518823>, 2018.
- McGill, M., Hlavka, D., Hart, W., Scott, V. S., Spinhirne, J., and Schmid, B.: Cloud Physics Lidar: instrument description and initial measurement results, *Appl. Optics*, 41, 3725–3734, <https://doi.org/10.1364/AO.41.003725>, 2002.
- Mishchenko, M. I.: *Electromagnetic Scattering by Particles and Particle Groups*, Cambridge University Press, New York, USA, <https://doi.org/10.1017/CBO9781139019064>, 2014.
- Mishchenko, M. I. and Travis, L. D.: Satellite retrieval of aerosol properties over the ocean using measurements of reflected sunlight: Effect of instrumental errors and aerosol absorption, *J. Geophys. Res.*, 102, 13543–13553, <https://doi.org/10.1029/97JD01124>, 1997.
- Mishchenko, M. I., Travis, L. D., Kahn, R. A., and West, R. A.: Modeling phase functions for dust-like tropospheric aerosols using a shape mixture of randomly oriented polydisperse spheroids, *J. Geophys. Res.*, 102, 16831–16847, <https://doi.org/10.1029/96JD02110>, 1997.
- Mishchenko, M. I., Cairns, B., Hansen, J. E., Travis, L. D., Burg, R., Kaufman, Y. J., Martins, J. V., and Shettle, E. P.: Monitoring of aerosol forcing of climate from space: analysis of measurement requirements, *J. Quant. Spectrosc. Ra.*, 88, 149–161, <https://doi.org/10.1016/j.jqsrt.2004.03.030>, 2004.
- Mishchenko, M. I., Cairns, B., Kopp, G., Schueler, C. F., Fafaul, B. A., Hansen, J. E., Hooker, R. J., Itchkawich, T., Maring, H. B., and Travis, L. D.: Accurate Monitoring of Terrestrial Aerosols and Total Solar Irradiance: Introducing the Glory Mission, *B. Am. Meteorol. Soc.*, 88, 677–691, <https://doi.org/10.1175/bams-88-5-677>, 2007.
- Mishchenko, M. I., Dlugach, J. M., and Liu, L.: Linear depolarization of lidar returns by aged smoke particles, *Appl. Optics*, 55, 9968–9973, <https://doi.org/10.1364/AO.55.009968>, 2016.
- Müller, D., Hostetler, C. A., Ferrare, R. A., Burton, S. P., Chernyakin, E., Kolgotin, A., Hair, J. W., Cook, A. L., Harper, D. B., Rogers, R. R., Hare, R. W., Cleckner, C. S., Obland, M. D., Tomlinson, J., Berg, L. K., and Schmid, B.: Airborne Multiwavelength High Spectral Resolution Lidar (HSRL-2) observations during TCAP 2012: vertical profiles of optical and microphysical properties of a smoke/urban haze plume over the northeastern coast of the US, *Atmos. Meas. Tech.*, 7, 3487–3496, <https://doi.org/10.5194/amt-7-3487-2014>, 2014.
- NASA: Airborne Science Data for Atmospheric Composition, ACEPOL, available at: <https://www-air.larc.nasa.gov/cgi-bin/ArcView/acepol>, last access: 22 January 2020.
- Navarro, R.: The NASA Earth Research-2 (ER-2) Aircraft: A Flying Laboratory for Earth Science Studies, Tech. rep. NASA/TM-2007-214615, available at: <https://ntrs.nasa.gov/search.jsp?R=20070014865> (last access: 22 January 2020), 2007.
- Nicolae, D., Nemuc, A., Müller, D., Talianu, C., Vasilescu, J., Bellegante, L., and Kolgotin, A.: Characterization of fresh and aged biomass burning events using multiwavelength Raman lidar and mass spectrometry, *J. Geophys. Res.-Atmos.*, 118, 2956–2965, <https://doi.org/10.1002/jgrd.50324>, 2013.
- O'Neill, N. T., Eck, T. F., Smirnov, A., Holben, B. N., and Thulasiraman, S.: Spectral discrimination of coarse and fine mode optical depth, *J. Geophys. Res.*, 108, 4559, <https://doi.org/10.1029/2002JD002975>, 2003.
- Rahman, H., Pinty, B., and Verstraete, M. M.: Coupled surface-atmosphere reflectance (CSAR) model: 2. Semiempirical surface model usable with NOAA advanced very high reso-

- lution radiometer data, *J. Geophys. Res.*, 98, 20791–20801, <https://doi.org/10.1029/93JD02072>, 1993.
- Rogers, R. R., Hair, J. W., Hostetler, C. A., Ferrare, R. A., Obland, M. D., Cook, A. L., Harper, D. B., Burton, S. P., Shinozuka, Y., McNaughton, C. S., Clarke, A. D., Redemann, J., Russell, P. B., Livingston, J. M., and Kleinman, L. I.: NASA LaRC airborne high spectral resolution lidar aerosol measurements during MILAGRO: observations and validation, *Atmos. Chem. Phys.*, 9, 4811–4826, <https://doi.org/10.5194/acp-9-4811-2009>, 2009.
- Russell, P. B., Kacenelenbogen, M., Livingston, J. M., Hasekamp, O. P., Burton, S. P., Schuster, G. L., Johnson, M. S., Knobelspiesse, K. D., Redemann, J., Ramachandran, S., and Holben, B.: A multiparameter aerosol classification method and its application to retrievals from spaceborne polarimetry, *J. Geophys. Res.-Atmos.*, 119, 9838–9863, <https://doi.org/10.1002/2013JD021411>, 2014.
- Schepers, D., van de Brugh, J. M. J., Hahne, P., Butz, A., Hasekamp, O. P., and Landgraf, J.: LINTTRAN v2.0: A linearised vector radiative transfer model for efficient simulation of satellite-born nadir-viewing reflection measurements of cloudy atmospheres, *J. Quant. Spectrosc. Ra.*, 149, 347–359, <https://doi.org/10.1016/j.jqsrt.2014.08.019>, 2014.
- Smit, J. M., Rietjens, J. H. H., van Harten, G., Noia, A. D., Laauwen, W., Rheingans, B. E., Diner, D. J., Cairns, B., Wasilewski, A., Knobelspiesse, K. D., Ferrare, R., and Hasekamp, O. P.: SPEX airborne spectropolarimeter calibration and performance, *Appl. Optics*, 58, 5695–5719, <https://doi.org/10.1364/AO.58.005695>, 2019.
- Snik, F., Karalidi, T., and Keller, C. U.: Spectral modulation for full linear polarimetry, *Appl. Optics*, 48, 1337–1346, <https://doi.org/10.1364/AO.48.001337>, 2009.
- Stamnes, S., Hostetler, C., Ferrare, R., Burton, S., Liu, X., Hair, J., Hu, Y., Wasilewski, A., Martin, W., Diedenhoven, B. V., Chowdhary, J., Cetinić, I., Berg, L. K., Stamnes, K., and Cairns, B.: Simultaneous polarimeter retrievals of microphysical aerosol and ocean color parameters from the “MAPP” algorithm with comparison to high-spectral-resolution lidar aerosol and ocean products, *Appl. Optics*, 57, 2394–2413, <https://doi.org/10.1364/AO.57.002394>, 2018.
- Stap, F. A., Hasekamp, O. P., and Röckmann, T.: Sensitivity of PARASOL multi-angle photopolarimetric aerosol retrievals to cloud contamination, *Atmos. Meas. Tech.*, 8, 1287–1301, <https://doi.org/10.5194/amt-8-1287-2015>, 2015.
- Stap, F. A., Hasekamp, O. P., Emde, C., and Röckmann, T.: Multiangle photopolarimetric aerosol retrievals in the vicinity of clouds: Synthetic study based on a large eddy simulation, *J. Geophys. Res.-Atmos.*, 121, <https://doi.org/10.1002/2016JD024787>, 2016.
- van Harten, G., de Boer, J., Rietjens, J. H. H., Di Noia, A., Snik, F., Volten, H., Smit, J. M., Hasekamp, O. P., Henzing, J. S., and Keller, C. U.: Atmospheric aerosol characterization with a ground-based SPEX spectropolarimetric instrument, *Atmos. Meas. Tech.*, 7, 4341–4351, <https://doi.org/10.5194/amt-7-4341-2014>, 2014.
- Waquet, F., Cairns, B., Knobelspiesse, K., Chowdhary, J., Travis, L. D., Schmid, B., and Mishchenko, M. I.: Polarimetric remote sensing of aerosols over land, *J. Geophys. Res.*, 114, D01206, <https://doi.org/10.1029/2008jd010619>, 2009.
- Waquet, F., Péré, J. C., Peers, F., Goloub, P., Ducos, F., Thieuleux, F., and Tanré, D.: Global detection of absorbing aerosols over the ocean in the red and near-infrared spectral region, *J. Geophys. Res.-Atmos.*, 121, 10902–10918, <https://doi.org/10.1002/2016JD025163>, 2016.
- Werdell, P. J., Behrenfeld, M. J., Bontempi, P. S., Boss, E., Cairns, B., Davis, G. T., Franz, B. A., Gliese, U. B., Gorman, E. T., Hasekamp, O., Knobelspiesse, K. D., Mannino, A., Martins, J. V., McClain, C. R., Meister, G., and Remer, L. A.: The Plankton, Aerosol, Cloud, ocean Ecosystem (PACE) mission: Status, science, advances, *B. Am. Meteorol. Soc.*, 100, 1775–1794, <https://doi.org/10.1175/BAMS-D-18-0056.1>, 2019.
- Winker, D. M., Pelon, J., Coakley, J. A., Ackerman, S. A., Charlson, R. J., Colarco, P. R., Flamant, P., Fu, Q., Hoff, R. M., Kittaka, C., Kubar, T. L., Le Treut, H., McCormick, M. P., Mégie, G., Poole, L., Powell, K., Trepte, C., Vaughan, M. A., and Wielicki, B. A.: The CALIPSO Mission, *B. Am. Meteorol. Soc.*, 91, 1211–1230, <https://doi.org/10.1175/2010BAMS3009.1>, 2010.
- Wu, L., Hasekamp, O., van Diedenhoven, B., and Cairns, B.: Aerosol retrieval from multiangle, multispectral photopolarimetric measurements: importance of spectral range and angular resolution, *Atmos. Meas. Tech.*, 8, 2625–2638, <https://doi.org/10.5194/amt-8-2625-2015>, 2015.
- Wu, L., Hasekamp, O., van Diedenhoven, B., Cairns, B., Yorks, J. E., and Chowdhary, J.: Passive remote sensing of aerosol layer height using near-UV multiangle polarization measurements, *Geophys. Res. Lett.*, 43, 8783–8790, <https://doi.org/10.1002/2016gl069848>, 2016.
- Wyzga, R. E. and Rohr, A. C.: Long-term particulate matter exposure: Attributing health effects to individual PM components, *J. Air Waste Manage.*, 65, 523–543, <https://doi.org/10.1080/10962247.2015.1020396>, 2015.
- Xu, F., van Harten, G., Diner, D. J., Kalashnikova, O. V., Seidel, F. C., Bruegge, C. J., and Dubovik, O.: Coupled retrieval of aerosol properties and land surface reflection using the Airborne Multiangle SpectroPolarimetric Imager, *J. Geophys. Res.-Atmos.*, 122, 7004–7026, <https://doi.org/10.1002/2017jd026776>, 2017.
- Xu, F., Harten, G. v., Diner, D. J., Davis, A. B., Seidel, F. C., Rheingans, B., Tosca, M., Alexandrov, M. D., Cairns, B., Ferrare, R. A., Burton, S. P., Fenn, M. A., Hostetler, C. A., Wood, R., and Redemann, J.: Coupled Retrieval of Liquid Water Cloud and Above-Cloud Aerosol Properties Using the Airborne Multiangle SpectroPolarimetric Imager (AirMSPI), *J. Geophys. Res.-Atmos.*, 123, 3175–3204, <https://doi.org/10.1002/2017JD027926>, 2018.
- Xu, F., Diner, D. J., Dubovik, O., and Schechner, Y.: A Correlated Multi-Pixel Inversion Approach for Aerosol Remote Sensing, *Remote Sensing*, 11, 746, <https://doi.org/10.3390/rs11070746>, 2019.
- Yorks, J. E., McGill, M. J., Scott, V. S., Wake, S. W., Kupchok, A., Hlavka, D. L., Hart, W. D., and Selmer, P. A.: The Airborne Cloud–Aerosol Transport System: Overview and Description of the Instrument and Retrieval Algorithms, *J. Atmos. Ocean. Tech.*, 31, 2482–2497, <https://doi.org/10.1175/JTECH-D-14-00044.1>, 2014.